Department of Exploration Geophysics

Spherical Wave AVO Response of Isotropic and Anisotropic Media: Laboratory Experiment versus Numerical Simulations

Mohammed Abdullah K Alhussain

This thesis is presented for the Degree of
Master of Science (Geophysics)
of
Curtin University of Technology

July 2007

Declaration

To the best of my knowledge and belief this thesis contains no material previously published by any other person except where due acknowledgment has been made.

This thesis contains no material which has been accepted for the award of any other degree or diploma in any university.

Signature:

Date:

ABSTRACT

A spherical wave AVO response is investigated by measuring ultrasonic reflection amplitudes from a water/Plexiglas interface. The experimental results show substantial deviation from the plane-wave reflection coefficients at large angles. However there is an excellent agreement between experimental data and full-wave numerical simulations performed with the reflectivity algorithm. By comparing the spherical-wave AVO response, modeled with different frequencies, to the plane-wave response, I show that the differences between the two are of such magnitude that three-term AVO inversion based on AVA curvature can be erroneous. I then propose an alternative approach to use critical angle information extracted from AVA curves, and show that this leads to a significant improvement of the estimation of elastic parameters.

Azimuthal variation of the AVO response of a vertically fractured model also shows good agreement with anisotropic reflectivity simulations, especially in terms of extracted critical angles which indicated that (1) reflection measurements are consistent with the transmission measurements; (2) the anisotropic numerical simulation algorithm is capable of simulating subtle azimuthal variations with excellent accuracy; (3) the methodology of picking critical angles on seismograms using the inflection point is robust, even in the presence of random and/or systematic noise.

ACKNOWLEDGMENTS

I give my sincerest gratitude to my supervisors, Dr. Milovan Urosevic and Professor Boris Gurevich for their inspiring ideas, their encouragement, patience and persistence in pursuing perfection of scientific research.

I would like to thank Professor Brian Evans, Dr. Bruce Hartley and Dr. Mark Lwin for their help with laboratory experiments and updating the operating software needed to perform adequate lab experiments.

Thank you British Geological Survey (BGS) for doing the anisotropic reflectivity modelling for me. Special thanks to Enru Liu in Edinburgh Anisotropy Project.

I also thank Abdullah Al Ramadhan and Marcos Grochau for their help and useful discussions throughout my project.

Finally, I thank my sponsor SAUDI ARAMCO for the Master's Degree scholarship.

TABLE OF CONTENTS

LIST OF FIGURES

LIST OF TABLES

LIST OF APPENDICES

CHAPTER 1
INTRODUCTION

1.1 Background

The seismic reflection method has been used for the last 50 years to delineate geological structure and stratigraphy, in order to understand the Earth's processes and to enable exploration and extraction of natural resources from the subsurface. The seismic method involves the transmission of a pulse of energy underground, which is then reflected at geological boundaries and discontinuities back to the surface. Sensors in the form of geophones may be used on land to pick-up the reflected energy and convert this to electrical signal, which is subsequently recorded and processed to produce an image of the geological subsurface.

Over recent years, there has been a growing expectation that such seismic data should yield not only an image of reflectors, but also provide information about the physical properties of the rocks. This has resulted in a major shift in seismic prospecting from structural imaging to reservoir characterization (Mavko, 2001). Knowledge of fracture direction, intensity and spatial distribution is of great importance for petroleum exploration. In many reservoirs, fractures control the permeability by providing conduits for fluid flow and hence can have a significant impact on hydrocarbon production. This is especially true in tight carbonate and low permeability reservoirs where essentially the only available means to extract hydrocarbons is to utilize the natural fractures (Thomsen, 2002; Mavko, 2001). In particular seismic prospecting is increasingly used to characterise naturally fractured reservoirs.

1.2 Spherical wave effect on AVO response

One of the most widely used tools in reservoir characterization is amplitude variation with offset (AVO) analysis. Most AVO analyses and inversion techniques employed today are based on the Zoeppritz equations for plane-wave reflection coefficients or their linearized approximations (Downton and Ursenbach, 2006). At the same time, seismic surveys use localized sources which produce spherical rather than plane waves, and it is

well known that the AVO response for the spherical waves differs from that of plane waves (Krail and Brysk, 1983). Winterstein and Hanten (1985) showed that the AVO amplitudes computed for non-planar (cylindrical) waves are much closer to real data than those provided by plane-wave modelling, especially for angles approaching the critical angle, where amplitude values are considerably lower than those which plane-wave theory predicts. More recent work by Haase (2004) highlighted the importance of accounting for spherical wave AVO effects in rock property estimations.

The use of the plane-wave approximation for reflection coefficients is usually justified by the fact that exploration target horizons are in the far field (depth usually exceeding 10-20 wavelengths) where wave-front curvature is small. This justification is adequate for moderate angles of incidence, well below the critical angle. Since the conventional (two-term) AVO analysis requires moderate offsets and angles, the use of the plane-wave Zoeppritz equations is justified.

At any given point of the interface, the reflection of the spherical wave involves reflection not just of one plane wave corresponding to the specular ray, but a range of plane waves corresponding to the bunch of rays within the ray beam around the central ray. Thus the amplitude of the reflected wave can be thought of as an average of plane wave reflection coefficient over a range of incident angles around the ray angle. When the variation of the plane wave reflection coefficient with incidence angle is gradual (as at angles below 20-25º), the averaging has very little effect. However, when the reflection coefficient changes rapidly, such as in the vicinity of the critical angle, the averaging smoothes over the reflection coefficient, causing the deviation of the reflection amplitude from the plane wave reflection coefficient. The magnitude of this effect depends on the averaging aperture which is controlled by the size of the Fresnel zone (and thus depends both on the frequency and distance between the source and the interface). In addition, at post-critical angles the curved wavefront generates a head wave, which forms a complex interference pattern with the post-critical reflection.

Conventional linear AVO analysis allows the extraction of two parameters, such as P- and S-wave impedance contrasts, and requires additional *a priori* information about the velocity-density relationship and/or Poisson's ratios. The introduction of longer receiver spreads and improved processing methods in recent years has enabled recording and preservation of long offset amplitudes. In principle, the use of these long offsets allows the extraction of three independent parameters, such as relative contrasts in compressional and shear velocities, V_P and V_S, and density ρ (Kelly et al. 2001). However, as shown by Haase (2004) and Van der Baan and Smit (2006), the plane-wave approximation becomes increasingly inaccurate for large incidence angles close to the critical angle, which makes the three-parameter inversion inadequate.

In this research, I verify the spherical wave effect on the AVO response by comparing the experimental results to full-wave numerical simulations. I show also what implication this effect has on three-term AVO inversion. According to various authors (Červený, 1961; Doruelo et al., 2006), one of the causes of the discrepancy between point source and plane-wave response is the interference of reflected waves with head waves. However, head waves can only be created by spherical (or cylindrical) waves; I include this effect in the broad term "spherical wave effect".

1.3 AVOaz response of a fractured medium

In recent years variations of the AVO response with azimuth (AVOaz response) have been increasingly used for the characterisation of fractured reservoirs. However up until now in many cases the interpretation of such multi-azimuthal data have been qualitative, and focused on estimating fracture and/or stress direction. With novel processing methods which enable preservation of the long offset data, quantitative interpretation becomes feasible. Quantitative interpretation requires a good understanding of the AVOaz response as a function of medium parameters.

One of the practical challenges of implementing long offset AVO-analysis is low signal-to-noise ratio where seismic wave propagates longer distances through the earth. Another challenge is phase changes especially close to critical angles which can cause serious

complications for accurate amplitude picking (Landro and Tsvankin, 2007). Water-column noise also can be a major challenge for exploiting long-offset seismic data which can distort reflected seismic signals (Landro, 2007).

Since azimuthal variation of AVO response is often more noticeable at large offsets (and can be rather weak), spherical wave effects must be carefully analysed and taken into account. This can be done either by full-wave numerical simulations (Karrenbach et al., 1997; Urdaneta, 1997; Landro and Tsvankin, 2007) or physical modeling in the laboratory (Fatkhan et al., 2001; Luo and Evans, 2004; Doruelo et al., 2006).

In this research these two approaches were combined by conducting an AVOaz laboratory experiment under fully controlled conditions, and numerically simulating this experiment. The AVOaz response was studied by physical modelling with a layered model simulating vertical fractures. Transmission measurements were performed to construct the elasticity tensor for the HTI model. This elasticity tensor is then used as an input into numerical simulations which were performed using an anisotropic full-wave reflectivity algorithm.

1.4 Research plan

The first part of this research discusses how the spherical wave can affect the AVO response and what implications it has on three term inversion. The second part explains the importance of accounting for azimuthal anisotropy and how the azimuthal variation of AVO response can be a powerful tool in quantifying fracture parameters. Chapter 2 gives the background theory required to understand anisotropy and amplitude variation with offset analysis. Chapter 3 demonstrates laboratory experiments performed to record both transmission and reflection measurements.

After that Chapter 4 explains the extraction of both the elastic constants of physical models and the anisotropic parameters of the HTI model. Chapter 5 shows how a spherical wave differs from that of a plane wave AVO response and what implications it

has in three-term AVO inversion. Chapter 6 analyses the AVOaz response for a water/HTI interface by comparing both laboratory measurements and numerical simulations. Conclusions and recommendations are discussed in Chapter 7.

CHAPTER 2
BACKGROUND THEORY

2.1 SIESMIC ANISOTROPY

2.1.1 Introduction

Traditional seismic theory is based on the assumption of an isotropic Earth. The concept of seismic isotropy assumes that seismic velocities in a homogeneous material are equal in all directions. In reality, most rocks are anisotropic. Seismic anisotropy is defined by Thomsen (2002) as "the dependence of velocity upon angle". The story of anisotropy started when McCollum and Snell (1932) discovered that some materials showed changes in P-wave velocity with measurement direction. In recent years anisotropy has been increasingly taken into account in processing and quantitative interpretation of seismic data. Due to its complexity, seismic anisotropy was ignored for a long time, and that was the main reason why geoscientists preferred to assume the isotropy of rocks and work with much simpler and intuitive equations. Processing the data under the assumption of an isotropic Earth was already a challenge and the cost of adding the complication of anisotropy must be justified by improvements in the final seismic image.

The advent of digital recording and long offset acquisition has enabled the quantification of seismic anisotropy. Better seismic data processing algorithms resulted in signal-to-noise improvement and more precise imaging of the subsurface. Powerful computers and more intuitive workstation interfaces made it possible to process and interpret data with great accuracy. For all of these reasons, seismic anisotropy has become an important subject which can't be neglected anymore.

The aim of this section is to present and explain the theory behind seismic anisotropy and anisotropic wave propagation concepts which are used in this research.

2.1.2 Causes of seismic anisotropy

Seismic anisotropy in a rock is caused by numerous geological processes which can be classified into three main categories: intrinsic, thin layering, and fracture-induced anisotropy (Crampin et. al., 1984). Each is now discussed in more detail:

Intrinsic anisotropy

A preferred orientation of anisotropic mineral grains is called "intrinsic anisotropy" (Thomsen, 1986). This type of anisotropy is widespread since it is typically found in shales which comprise 70% of all sedimentary rocks (Slater, 1997), where the micro-alignment of plate-like mineral grains due to compaction, stresses or sedimentation during deposition makes them intrinsically anisotropic. These minerals can also themselves be intrinsically anisotropic. For that reason, shales possess a high degree of anisotropy where the velocity difference along and across the plate-lets is big. A microscopic image of a shale formation is shown in Figure 2.1.

Thin layering

This type of anisotropy is typical for a thinly layered sedimentary sequence which is commonly found in all sand-shale environments. The seismic wavelet has to be much larger than the layering, where the sequence of isotropic layers is effectively "averaged" by the long seismic wavelength, appearing as a homogeneous equivalent anisotropic medium or effective medium (Thomsen, 2002). Backus (1962) showed that for long waves such thinly layered media is equivalent to a transversely isotropic (TI) homogeneous medium (The isotropic and anisotropic symmetry classes are discussed later in this chapter). This type of anisotropy is also known as long wavelength anisotropy.

Fracture-induced anisotropy

The non uniform action of stress, where the two principal horizontal stresses are not equal, will cause the rock to fracture and deformation is commonly aligned with the dominant horizontal stress direction. Fracture-induced anisotropy plays an important role

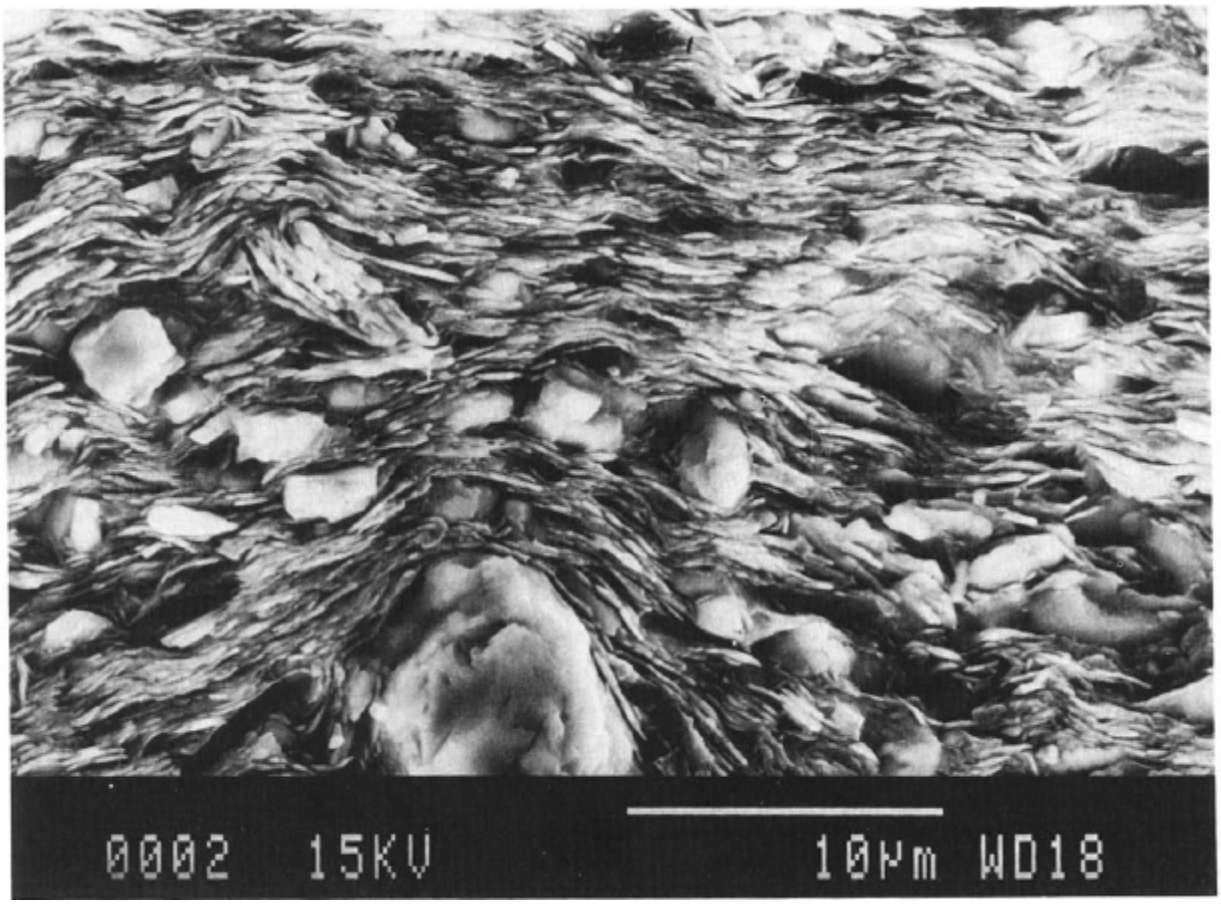

Figure 2.1 A microscopic vertical section of shale showing what shale looks like at the grain scale. The plate-like particles are clay minerals while the larger, nearly spherical particles are silt (after Hornby et al., 1994).

in exploration for hydrocarbons, because it can be used to infer the direction of fractures in a reservoir. At depth, due to litho-static stress, sub-horizontal or horizontal fractures usually close. On the contrary, sub-vertical or vertical fractures may open and become important to hydrocarbon exploration since they will be the main source of permeability especially in low porosity, tight reservoirs (Figure 2.2).

2.1.3 Anisotropy and heterogeneity

There are two important distinctions between anisotropy and heterogeneity. The first one is that anisotropy is the variation in vectorial value with direction at one point, whereas, heterogeneity is the variation in vectorial or scalar values between two or more points. The second distinction between anisotropy and heterogeneity is that anisotropy tends to describe mainly physical properties. On the other hand, heterogeneity is typically used to describe point-to-point variations in compositions, geometries or physical properties. Thomsen (2002) discussed the difference between anisotropy and heterogeneity, where at the small scale (the seismic wavelet is small compared to the rocks), heterogeneity is measured. In the contrary, the rock appears anisotropic in the large scale (where the seismic wavelet is much larger than the propped rocks).

According to Gassmann (1964), there are four possible types of rocks. The first type is an isotropic-homogeneous rock, where the velocity neither changes with direction nor with position. The second type is an isotropic-heterogeneous rock where the velocity does not change with direction but with position. The third type is an anisotropic-homogeneous rock which is very important to seismic exploration since the long seismic wavelet which propagates through hydrocarbon reserves sees the rock as anisotropic and homogeneous. The final type is an anisotropic-heterogeneous rock where velocity changes with both direction and position (Figure 2.3).

2.1.4 The theory of elasticity and Hooke's Law

Elasticity is the property that enables a fluid or solid body to return to its original shape after removal of a distorting stress (Sheriff, 1991). It is the elastic properties of rocks that allow seismic waves to propagate through the Earth and for that reason the concept of

Figure 2.2 Near vertical fractures from an outcrop, Central Saudi Arabia.

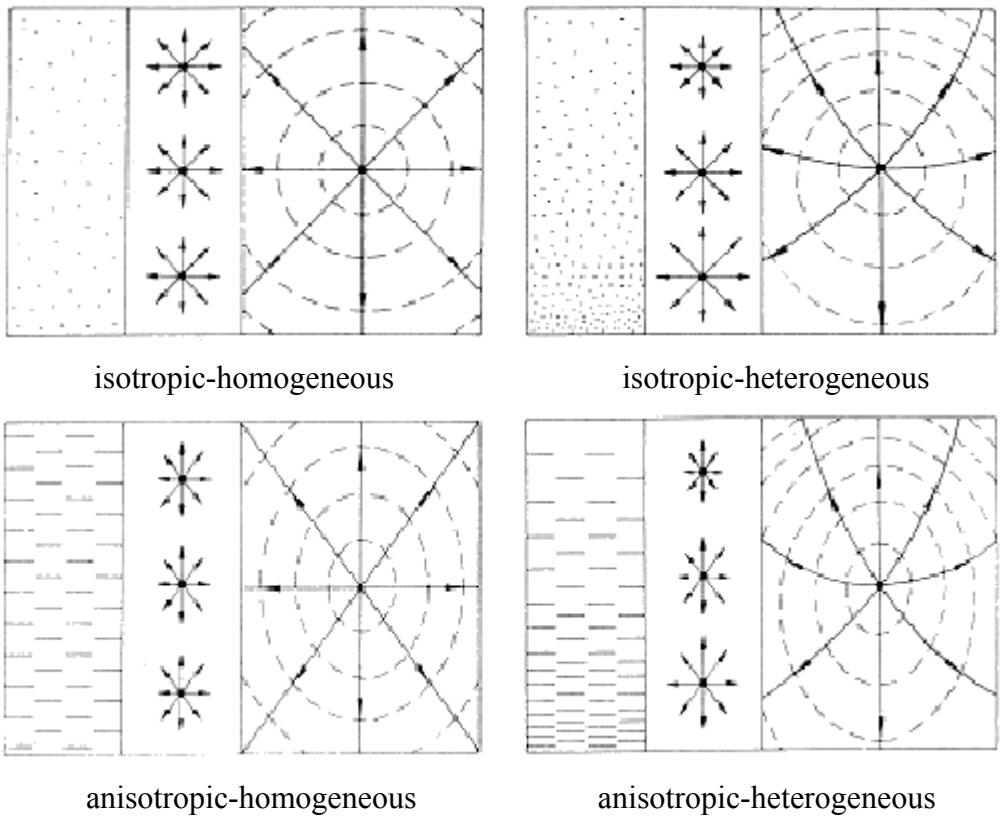

Figure 2.3 Illustration of the terms isotropy - anisotropy and homogeneity – inhomogeneity (after Gassmann, 1964).

elasticity is important to seismology. Stress is defined as a force per unit area, while strain is the deformation resulting from that stress. In the case of isotropic, linear elastic material, the relationship between stress and strain can be express by the isotropic form of Hooke's Law as (Timoshenko and Goodier, 1934):

$$\sigma_{ij} = 2\mu\varepsilon_{ij} + \lambda\varepsilon_{kk}\delta_{ij}\,, \tag{2.1}$$

where σ_{ij} = elements of stress tensor, ε_{ij} = element of strain tensor, ε_{kk} = volumetric strain (sum over repeated index), δ_{ij} = 0 if i ≠ j, and 1 if i = j, λ and μ called Lamé constants.

Hooke's law for isotropic, linear elastic material can be written in matrix form as follows:

$$\begin{bmatrix}\sigma_1\\ \sigma_2\\ \sigma_3\\ \sigma_4\\ \sigma_5\\ \sigma_6\end{bmatrix} = \begin{bmatrix}\lambda+2\mu & \lambda & \lambda & 0 & 0 & 0\\ \lambda & \lambda+2\mu & \lambda & 0 & 0 & 0\\ \lambda & \lambda & \lambda+2\mu & 0 & 0 & 0\\ 0 & 0 & 0 & \lambda & 0 & 0\\ 0 & 0 & 0 & 0 & \lambda & 0\\ 0 & 0 & 0 & 0 & 0 & \lambda\end{bmatrix} \times \begin{bmatrix}\varepsilon_{11}\\ \varepsilon_{22}\\ \varepsilon_{33}\\ 2\varepsilon_{23}\\ 2\varepsilon_{31}\\ 2\varepsilon_{12}\end{bmatrix}. \tag{2.2}$$

Hooke's law for general anisotropic, linear elastic solids states that each component of the stress tensor is a linear combination of all components of strains, and vice versa (Mavko et al., 1998),

$$\sigma_{ij} = c_{ijkl}\varepsilon_{kl}\ . \tag{2.3}$$

In the relation (2.3), the summation is implied over the repeated subscripts *k* and *l*. c_{ijkl} is called the elastic stiffness tensor which is a fourth rank tensor obeying the laws of tensor transformation and has a total of eighty-one components. The good thing is that not all of the 81 components are independent, due to the symmetry of stress and strain which implies that: $c_{ijkl} = c_{jikl} = c_{ijlk} = c_{jilk}$ resulting in only thirty-six independent constants. The total number of independent constants further reduces to twenty-one due to strain energy considerations where $c_{ijkl} = c_{klij}$.

The elasticity tensor has four indices *i*, *j*, *k* and *l*, two of which correspond to the indices of stress, and two to the indices of strain. The fourth-order elasticity tensor can be

represented by a two dimensional matrix because of the symmetry of stress. As a result, the 3x3x3x3 tensor is replaced by a 6x 6 matrix as follows (Mavko et al., 1998; Thomsen, 2002):

$$C_{ij=}\begin{bmatrix} C_{11}C_{12}C_{13}C_{14}C_{15}C_{16} \\ C_{21}C_{22}C_{23}C_{24}C_{25}C_{26} \\ C_{31}C_{32}C_{33}C_{34}C_{35}C_{36} \\ C_{41}C_{42}C_{43}C_{44}C_{45}C_{46} \\ C_{51}C_{52}C_{53}C_{54}C_{55}C_{56} \\ C_{61}C_{62}C_{63}C_{64}C_{65}C_{66} \end{bmatrix}. \tag{2.4}$$

The new 6x6 matrix is symmetrical about the main diagonal which reduces the independent constants to only 21. The most general kind of anisotropy has at most 21 different matrix elements which are almost impossible to measure in any geophysical field survey. Fortunately, what we see in seismic data is much simpler case.

2.1.5 Symmetry classes

Due to the symmetry in any material, the total number of elastic constants is reduced proportionally to the degree of symmetry. Ebrom and Sheriff (1992) stated that there are possibly seven different types of elastic anisotropy which are named after equivalent crystal types (Figure 2.4).

Isotropic symmetry

The simplest symmetry case is an isotropic material where both P-wave and S-wave velocities are the same in all directions. As a result, the number of independent elastic constants is reduced to only two. The resulting stiffness matrix is as follows:

$$C_{ij=}\begin{bmatrix} C_{11} & C_{12} & C_{12} & 0 & 0 & 0 \\ C_{12} & C_{11} & C_{12} & 0 & 0 & 0 \\ C_{12} & C_{12} & C_{11} & 0 & 0 & 0 \\ 0 & 0 & 0 & C_{44} & 0 & 0 \\ 0 & 0 & 0 & 0 & C_{44} & 0 \\ 0 & 0 & 0 & 0 & 0 & C_{44} \end{bmatrix}, C_{12} = C_{11} - 2C_{44}. \tag{2.5}$$

SYSTEM	UNIT CELL	ANGLES	EDGES	ELASTIC CONSTANTS
TRICLINIC	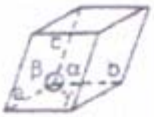	$\alpha \neq \beta \neq \gamma \neq 90^\circ$	$a \neq b \neq c$	21
MONOCLINIC	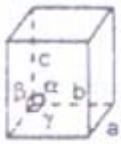	$\alpha = \gamma = 90^\circ$ $\beta > 90^\circ$	$a \neq b \neq c$	13
ORTHORHOMBIC	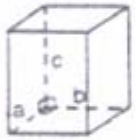	$\alpha = \beta = \gamma = 90^\circ$	$a \neq b \neq c$	9
TRIGONAL	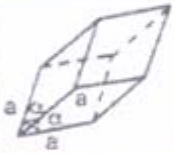	$\alpha = \beta = \gamma \neq 90^\circ$	$a = b = c$	7
TETRAGONAL		$\alpha = \beta = \gamma = 90^\circ$	$a = b \neq c$	7
HEXAGONAL	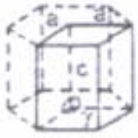	$\alpha = \beta = 90^\circ$ $\gamma = 120^\circ$	$a = b \neq c$	5
CUBIC	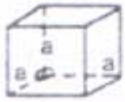	$\alpha = \beta = \gamma = 90^\circ$	$a = b = c$	3

Figure 2.4 Seven possible types of anisotropy and the number of elastic constants needed to characterize an anisotropic velocity field (after Ebrom and Sheriff, 1992).

Lamé's parameters λ and μ are directly related to C_{ij} elements according to these equations:

$$C_{11} = \lambda + 2\mu, C_{44} = \mu, C_{12} = \lambda . \quad (2.6)$$

2.1.6 Transverse isotropy

Transverse isotropy, or TI for short, is the most common anisotropic model in exploration seismology, since shale formations which comprise about 70% of sedimentary crust are considered as TI media (Tsvankin, 2001).

Transverse isotropy is classified according to the symmetry axis. If the axis is vertical, we have vertical transverse isotropy or VTI. This type of anisotropy is very common since shale formations are VTI media. Rotating the access of symmetry from vertical to horizontal will result in horizontal transverse isotropy or HTI medium. The combination of both VTI and HIT media will give a more complicated type of anisotropy called orthorhombic media. All three types are shown in Figure 2.5.

Detecting and quantifying this type of anisotropy is important for correlation purposes, such as comparing sonic logs in vertical and deviated wells, and for borehole and surface seismic imaging and studies of amplitude variation with offset (Armstrong et. al., 1995).

As a transversely isotropic medium has more complex velocity structure than an isotropic medium, it also has a more complex stiffness matrix. The TI media requires five independent elastic constants to express Hooke's low (White, 1965).

Vertical transverse isotropy (VTI)

In order to reduce the ambiguity involved in naming an anisotropic medium 'isotropic', this kind of TI medium can also be called polar anisotropy (Thomsen, 2002). The stiffness matrix for a VTI medium is (Mavko et al., 1998):

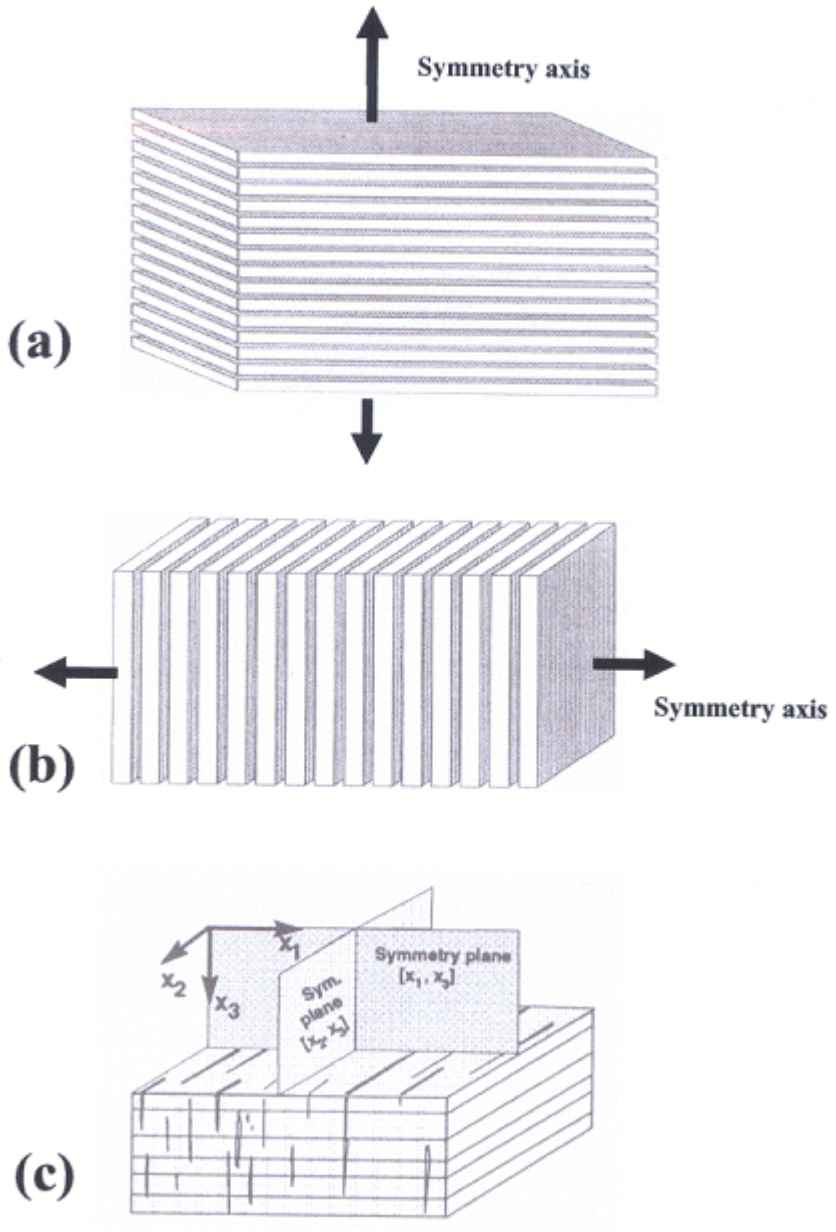

Figure 2.5 Illustrations of three anisotropic media with different axes of symmetry. (a) Transverse isotropy with vertical symmetry (VTI), (b) transverse isotropy with horizontal symmetry (HTI) and (c) orthorhombic anisotropy with two sets of symmetrical planes (after Rüger, 1996).

$$C^{(VTI)}_{ij=}\begin{bmatrix} C_{11} & C_{12} & C_{13} & 0 & 0 & 0 \\ C_{12} & C_{11} & C_{13} & 0 & 0 & 0 \\ C_{13} & C_{13} & C_{33} & 0 & 0 & 0 \\ 0 & 0 & 0 & C_{44} & 0 & 0 \\ 0 & 0 & 0 & 0 & C_{44} & 0 \\ 0 & 0 & 0 & 0 & 0 & C_{66} \end{bmatrix}, C_{66} = \frac{1}{2}(C_{11} - C_{12}). \qquad (2.7)$$

Horizontal transverse isotropy (HTI)

Naturally occurring fracture systems in the Earth is the most common cause of azimuthal anisotropy (variation of seismic properties with azimuth). Studying the azimuthal anisotropy is of great importance in exploring for hydrocarbons because it can be a useful tool to gain information about the orientation of fractures, their size and the nature of crack in-fill, which can be used to gain a detailed characterization of subsurface reservoirs and predictions of possible fluid pathways.

Figure 2.6 shows a sketch of an HTI model where the symmetry axis is horizontal and the [x1,x3]-plane is called the symmetry-axis plane. Waves confined to the plane normal to the symmetry axis do not exhibit any velocity variations with propagation angle; this plane is called the isotropy plane or fracture plane. Shear-wave splitting (birefringence) which is caused by fracture-induced azimuthal anisotropy can be seen in Figure 2.5 where the S-wave splits into two polarized waves; one has particle motion parallel to the fractures (polarized within the isotropy plane) travelling with relatively fast velocity (S^{II}) and the other has particle motion perpendicular to the fracture (polarized within the symmetry-axis plane) with relatively slower velocity ($S^{\perp}$) (Martin and Davis, 1987; Rüger, 1996).

The stiffness matrix for an HTI medium is:

$$C^{(HTI)}_{ij=}\begin{bmatrix} C_{11} & C_{13} & C_{13} & 0 & 0 & 0 \\ C_{13} & C_{33} & C_{33}-2C_{44} & 0 & 0 & 0 \\ C_{13} & C_{33}-2C_{44} & C_{33} & 0 & 0 & 0 \\ 0 & 0 & 0 & C_{44} & 0 & 0 \\ 0 & 0 & 0 & 0 & C_{55} & 0 \\ 0 & 0 & 0 & 0 & 0 & C_{55} \end{bmatrix}. \qquad (2.8)$$

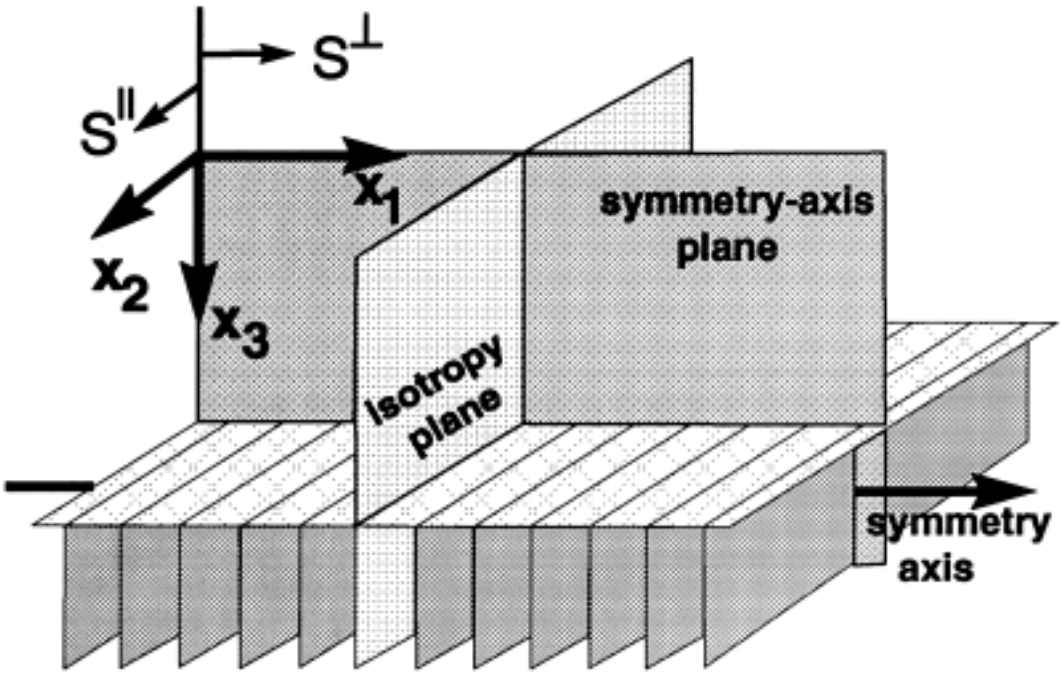

Figure 2.6 HTI model due to a system of parallel vertical cracks. Vertically travelling shear waves in HTI media split into two modes polarization parallel and perpendicular to the crack faces (after Rüger, 1996).

2.1.7 Thomsen's Elastic Anisotropy

Thomsen (1986) pointed out that in most cases of interest to geophysicists, the anisotropy is weak (<10-20 percent) allowing the complex anisotropic equations to simplify considerably. The stiffness-coefficient notation is inconvenient for developing analytical insight into how anisotropy influences wave propagation and reflection moveout. Thomsen's notation simplifies the explanation, and his parameters are, in most cases, well suited for quantifying the effect of anisotropy on wave propagation. His idea is to separate the influence of the anisotropy from the "isotropic" quantities chosen as the P- and S-wave velocities along the axis of symmetry. The five elastic constants of TI media can be replaced by the vertical velocities V_{P0} and V_{S0} (P- and S velocities respectively), three dimensionless anisotropic parameters, denoted as ε, δ and γ (Thomsen, 1986):

$$V_{P0} = \alpha = \sqrt{\frac{C_{33}}{\rho}}, \tag{2.9}$$

$$V_{S0} = \beta = \sqrt{\frac{C_{44}}{\rho}}, \tag{2.10}$$

$$\varepsilon = \frac{C_{11} - C_{33}}{2C_{33}}, \tag{2.11}$$

$$\gamma = \frac{C_{66} - C_{44}}{2C_{44}}, \tag{2.12}$$

$$\delta = \frac{(C_{13} + C_{44})^2 - (C_{33} - C_{44})^2}{2C_{33}(C_{33} - C_{44})}. \tag{2.13}$$

For VTI media, the constant ε describes the fractional difference of the P-wave velocities in the vertical and horizontal directions (P-wave anisotropy). Similarly, the constant γ describes the fractional difference of SH-wave velocities between vertical and horizontal directions (S-wave anisotropy). The δ parameter is responsible for the angular dependence of V_P in the vicinity of the vertical (symmetry) direction (Tasvankin, 2001).

If the anisotropy is weak, the phase velocities can be written conveniently in terms of Thomsen's notations as (Mavko et. al., 1998):

$$V_P(\theta) \approx \alpha(1+\delta\sin^2\theta\cos^2\theta+\varepsilon\sin^4\theta), \tag{2.14}$$

$$V_{SV}(\theta) \approx \beta[1+(\frac{\alpha^2}{\beta^2})(\varepsilon-\delta)\sin^2\theta\cos^2\theta], \tag{2.15}$$

$$V_{SH}(\theta) \approx \beta(1+\gamma\sin^2\theta), \tag{2.16}$$

where V_P is the pseudo-longitudinal wave, V_{SH} is the wavefront velocity of the pure shear wave, V_{SV} is the pseudo-shear wave polarized normal to the pure shear wave, θ is the phase angle between the wavefront normal and the axis of symmetry. The elastic constants of a transversely isotropic elastic medium can be characterized conveniently using Thomsen's notation for weak elastic anisotropy. For that reason, it is widely used in seismology.

2.1.8 Thomsen's notations for HTI media

Thomsen's parameters ε, γ and δ were generically derived with respect to a horizontal plane which are suitable to describe VTI media. Rüger (1996) introduced a new form of Thomsen's notation for HTI media where he stated that P- and SV-wave propagation in the symmetry-axis plane of HTI media can be described by the known VTI equations using the elastic stiffness components C_{ij} or, alternatively, using Thomsen's parameters ε^{v} and δ^{v} defined with respect to the vertical plane in the same way as in VTI media:

$$\varepsilon^{(v)} = \frac{C_{11}-C_{33}}{2C_{33}}, \tag{2.17}$$

$$\delta^{(v)} = \frac{(C_{13}+C_{55})^2-(C_{33}-C_{55})^2}{2C_{33}(C_{33}-C_{55})}, \tag{2.18}$$

The new Thomsen's parameters $\varepsilon^{(v)}$, $\gamma^{(v)}$ and $\delta^{(v)}$ can be expressed through the generic Thomsen's parameters using the following relations:

$$\varepsilon^{(v)} = \frac{-\varepsilon}{1+2\varepsilon}, \tag{2.19}$$

$$\gamma^{(v)} = \frac{-\gamma}{1+2\gamma}, \tag{2.20}$$

$$\delta^{(v)} = \frac{\delta - 2\varepsilon(1+\frac{\varepsilon}{f})}{(1+2\varepsilon)(1+\frac{2\varepsilon}{f})}, \tag{2.21}$$

where $f = 1-(V_{S0}/V_{P0})^2$ and both V_{S0} and V_{P0} are measured along the horizontal symmetry axis.

2.2 THEORY OF TRANSMISSION AND REFLECTION

2.2.1 Partitioning of energy at an interface

When a sound wave propagating through a solid reaches a boundary with another solid of different properties, it will partly reflect off the boundary at some angle and partly pass through it, but have a different direction after the boundary than before it. Zoeppritz (1919) published the solution to the reflection and transmission of plane waves at a plane boundary between two isotropic media. In his derivation of what is now called "The Zoeppritz equations", he assumed the continuity of stress and displacement at the reflecting horizon. The incident P-wave on a boundary between two layers of different velocities and densities will give rise to a reflected P-wave, a reflected S-wave, a transmitted P-wave and a transmitted S-wave. The difference in velocities and densities between the upper and lower layers (1 and 2) cause the angle of reflected P-wave (φ_1) energy to differ from the angle of transmitted P-wave energy (φ_2). Similarly, the angle of incident S-wave energy (ψ_1) is different from the angle of transmitted S-wave energy (ψ_2) (Figure 2.7).

It is convenient to work with displacement potentials instead of the displacement vector **u** when dealing with wave propagation problems (Officer, 1958). The two displacement potentials are defined as a compressional-wave potential ϕ and a shear-wave potential ψ in terms of the displacement **u** and **w** as:

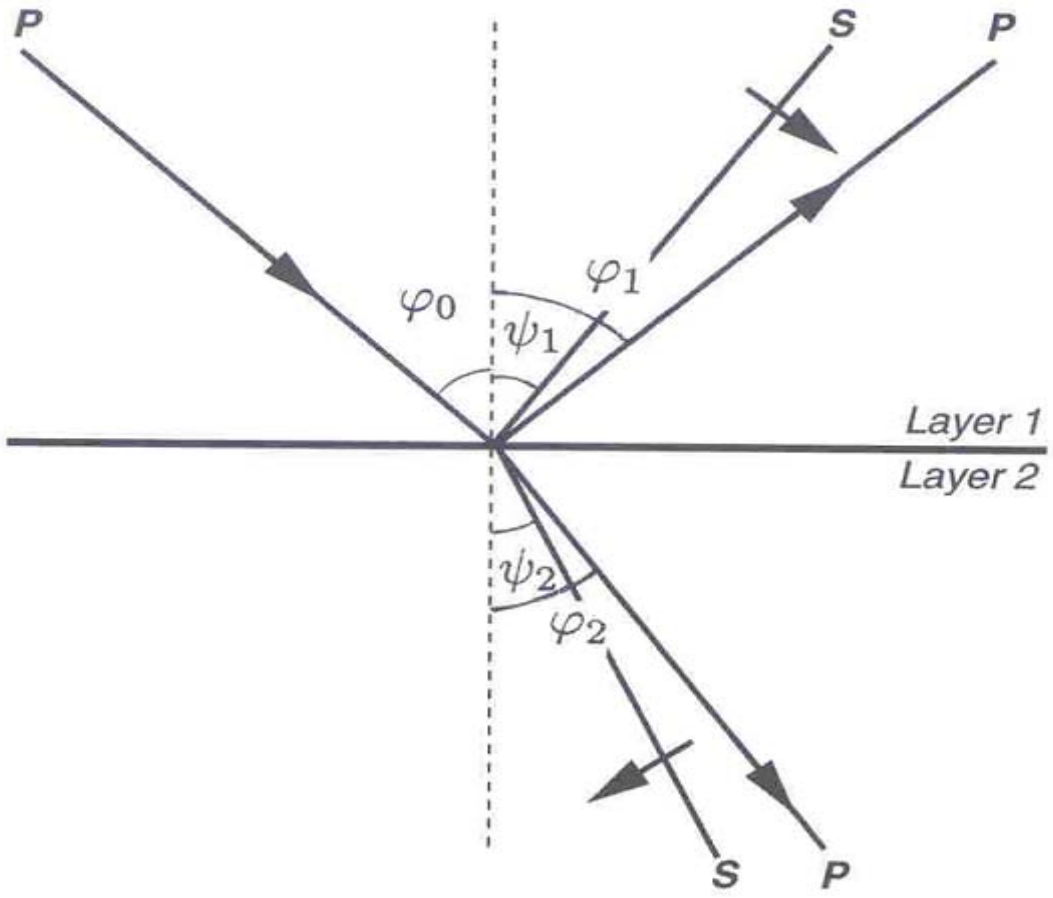

Figure 2.7 Incident P-wave and associated reflected and transmitted P- and S-waves. The arrows indicate the difference between reflected and transmitted angles (after Yilmaz, 1986).

$$\mathbf{u} = \frac{\partial \phi}{\partial x} + \frac{\partial \psi}{\partial z}, \tag{2.22}$$

$$\mathbf{w} = \frac{\partial \phi}{\partial z} - \frac{\partial \psi}{\partial x}. \tag{2.23}$$

There are four important boundary conditions used to derive Zoeppritz's equations:

1 .The displacement component tangential to the interface is continuous: $u_1 = u_2$.

2. The displacement component normal to the interface is continuous: $\omega_1 = \omega_2$.

3. The stress component normal to the interface is continuous: $(P_{zz})_1 = (P_{zz})_2$.

4. The stress component tangential to the interface is continuous: $(P_{xz})_1 = (P_{xz})_2$.

Each of these boundary conditions is used to derive one equation and in total we have four equations known as the Zoeppritz's equations which are expressed in matrix format as follows (Yilmaz, 1987):

$$\begin{bmatrix} \cos\varphi_1 & \frac{\alpha_1}{\beta_1}\sin\psi_1 & \frac{\alpha_1}{\alpha_2}\cos\varphi_2 & -\frac{\alpha_1}{\beta_2}\sin\psi_2 \\ -\sin\varphi_1 & \frac{\alpha_1}{\beta_1}\cos\psi_1 & \frac{\alpha_1}{\alpha_2}\sin\varphi_2 & \frac{\alpha_1}{\beta_2}\cos\psi_2 \\ -\cos 2\psi_1 & -\sin 2\psi_1 & \frac{\rho_2}{\rho_1}\cos 2\psi_2 & -\frac{\rho_2}{\rho_1}\sin 2\psi_2 \\ \sin 2\varphi_1 & -\frac{\alpha^2{}_1}{\beta^2{}_1}\cos 2\psi_1 & \frac{\rho_2\beta_2{}^2\alpha_1{}^2}{\rho_1\beta_1{}^2\alpha_2{}^2}\sin 2\varphi_2 & \frac{\rho_2\alpha_1{}^2}{\rho_1\beta_1{}^2}\cos 2\psi_2 \end{bmatrix} \begin{bmatrix} A_1 \\ B_1 \\ A_2 \\ B_2 \end{bmatrix} = \begin{bmatrix} \cos\varphi_1 \\ \sin\varphi_1 \\ \cos 2\psi_1 \\ \sin 2\varphi_1 \end{bmatrix}. \tag{2.24}$$

2.2.2 Amplitude variation with offset in isotropic media

Zoeppritz's equations relate reflection coefficients as a function of the angle of incidence to medium physical parameters. For that reason, Zoeppritz's equations are the building blocks for AVO analysis. The variation of P-wave amplitude with incidence angle is an important tool as a direct hydrocarbon indicator. For example, in comparison to the

surrounding lithology, a gas saturated formation exhibits lower acoustic impedance. Algebraic complexity and a requirement for information usually not available, made the Zoeppritz's equations not practical for AVO analysis. Therefore, conventional AVO analysis is mostly based on approximate analytic expressions for reflection coefficients.

Bortfeld (1961) was the first to approximate Zoeppritz equations for P-to-P reflection amplitude which is given as:

$$R(\theta_1) = \frac{1}{2}\ln\left(\frac{\alpha_2 \rho_2 \cos\theta_2}{\alpha_1 \rho_1 \cos\theta_1}\right) + \left(2 + \frac{\ln\left(\frac{\rho_2}{\rho_1}\right)}{\ln\left(\frac{\alpha_2}{\alpha_1}\right) - \ln\left(\frac{\alpha_2 \beta_1}{\alpha_1 \beta_2}\right)}\right) \frac{\beta^2{}_1 - \beta^2{}_2}{\alpha^2{}_1} \sin^2\theta_1, \quad (2.25)$$

where θ_1 and θ_2 are incident and transmitted angles respectively, α is P-wave velocity, β is S-wave velocity, ρ is density, the subscripts 1 and 2 denotes the upper and lower media.

In his approximation, Bortfeld arranged the equation into two terms separating the acoustic and the elastic effects on reflection amplitudes but its practical implementation for AVO analysis has not been considered because it does not explicitly indicate angle or offset dependence of reflection amplitudes (Yilmaz, 1987). The first practical application of AVO analysis was possible after the introduction of the Aki-Richard's approximation assuming that changes in elastic properties of rocks across the layer boundary are small and propagation angles are within the sub-critical range (Aki and Richard, 1980). The resulting equation can be written as follows:

$$R(\theta) = \left[\frac{1}{2}\left(1 + \tan^2\theta\right)\right]\frac{\Delta\alpha}{\alpha} - \left[4\frac{\beta^2}{\alpha^2}\sin^2\theta\right]\frac{\Delta\beta}{\beta} + \left[\frac{1}{2}\left(1 - 4\frac{\beta^2}{\alpha^2}\sin^2\theta\right)\right]\frac{\Delta\rho}{\rho}, \quad (2.26)$$

where $\alpha = (\alpha_1 + \alpha_2)/2$, average P-wave velocity and $\Delta\alpha = (\alpha_2 - \alpha_1)$, $\beta = (\beta_1 + \beta_2)/2$, average S-wave velocity and $\Delta\beta = \beta_2 - \beta_1$, $\rho = (\rho_1 + \rho_2)/2$, average density and

$\Delta\rho = \rho_2 - \rho_1$, and $\theta = (\varphi_1 + \varphi_2)/2$, average of the incidence and transmission angles for the P-wave.

Shuey (1985) derived a more practical form of Aki-Richards equation where he separated the equation into three reflection terms as follows:

$$\mathrm{R}(\theta) = R_p + G\sin^2\theta + C\tan^2\theta\sin^2\theta, \tag{2.27}$$

where

$$R_p = \left[\frac{1}{2}\left(\frac{\Delta\alpha}{\alpha} + \frac{\Delta\rho}{\rho}\right)\right],$$

$$G = \left[\frac{1}{2}\frac{\Delta\alpha}{\alpha} - 4\frac{\beta^2}{\alpha^2}\frac{\Delta\beta}{\beta} - 2\frac{\beta^2}{\alpha^2}\frac{\Delta\rho}{\rho}\right],$$

$$C = \left[\frac{1}{2}\frac{\Delta\alpha}{\alpha}\right].$$

R_p is called the intercept, G is the gradient and C is the curvature term usually dealing with large incident angles.

The comparison between the Zoeppritz equation, the Bortfeld and Aki-Richards approximations is shown in Figure 2.7. The upper and lower media were interchanged to give Figure 2.8 a and b (Smith and Gidlow, 1987). Although the elastic properties in the upper and lower medium differ by small amount, the variation of amplitude with angle of incidence relative to normal incidence can be considerable. For pre-critical incident angles, these approximations closely follow the exact solution.

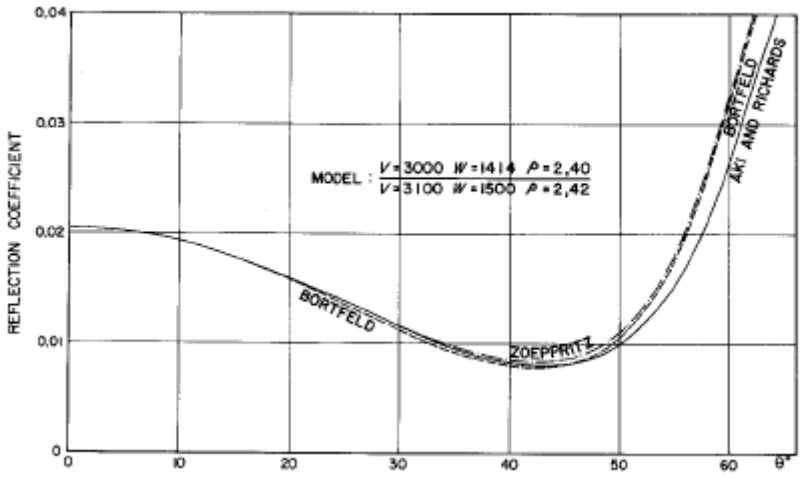

(a)

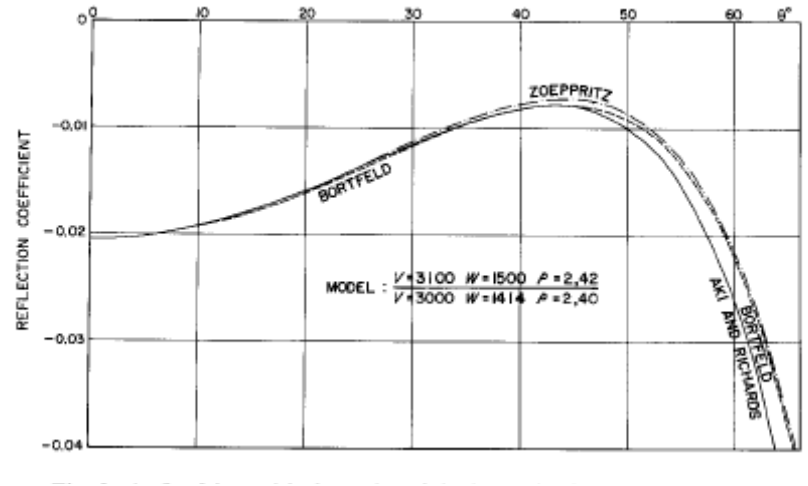

(b)

Figure 2.8 P-to-P AVO using the exact Zeoppritz equation, Bortfeld and Aki-Richards (after Smith and Gidlow, 1987).

2.2.3 Amplitude variation with offset in azimuthally anisotropic media

Reflection coefficient approximations given by Bortfeld (1961), Aki and Richard (1980), and Shuey (1985) (equations 2.25 to 2.27) do not account for anisotropy. Vertical fractures, which often cause azimuthal anisotropy, affect hydrocarbon flow in reservoirs. For that reason, it is necessary to include azimuthal anisotropy into calculations of reflection amplitudes. Interpreting AVO results assuming the isotropy of rocks could result in significant errors (Teng and Mavko, 1996).

Plane waves in HTI medium

If a plane P-wave is incident on an HTI medium outside of the symmetry-axis and isotropy plane, three plane waves are generated. The first one is a P-wave polarized approximately along its propagation direction. The second and third are two S-waves, one is polarized within the isotropy plane, referred to as S-parallel ($S^{\parallel}$), and the other one is polarized in the symmetry axis, referred to as S perpendicular ($S^{\perp}$), Polarization of S-waves in the direction parallel and perpendicular to fractures (S-wave birefringence) is often used as a valuable tool for fractured reservoir exploration and development (Martin and Davis, 1987).

Rüger's approximations

Analysis of amplitude variations with offset and azimuth (AVOaz) often caused by vertical fractures is an important tool in inferring medium elastic parameters from surface seismic. For long wavelengths, a fractured reservoir can be represented by the HTI model. The PP-wave reflection coefficient R at a horizontal interface between isotropic and HTI media is defined by the approximate formula (Rüger, 1996):

$$R_p(i,\phi) = \frac{1}{2}\frac{\Delta Z}{\overline{Z}} + \frac{1}{2}\left\{\frac{\Delta\alpha}{\overline{\alpha}} - \left(\frac{2\overline{\beta}}{\overline{\alpha}}\right)^2 \frac{\Delta G}{\overline{G}} + \left[\Delta\delta^{v} + s\left(\frac{2\overline{\beta}}{\overline{\alpha}}\right)^2 \Delta\gamma\right]\cos^2\phi\right\}\sin^2 i + \frac{1}{2}\left\{\frac{\Delta\alpha}{\overline{\alpha}} + \Delta\varepsilon^{v}\cos^4\phi + \Delta\delta^{v}\sin^2\phi\cos^2\phi\right\}\sin^2 i\tan^2 i, \tag{2.28}$$

where i is the angle between the slowness vector of the incident wave and the vertical, ϕ is the azimuthal angle defined with respect to the symmetry axis pointing in the x_1-

direction (see Figure 2.9), $Z = \rho\alpha$ is the vertical P-wave impedance and $G = \rho\beta^2$ is the vertical shear modulus. The elastic parameters are expressed through their average values and relative differences across the interface. The vertical P-wave velocities in the upper and lower layers, for example, can be written as functions of the average velocity $\overline{\alpha} = \frac{1}{2}(\alpha_2 + \alpha_1)$ and the difference $\Delta\alpha = (\alpha_2 - \alpha_1)$. Corresponding expressions are defined for the shear modulus, the density and the P-wave impedance.

The superscript "*v*" in equation 2.28 emphasizes that the coefficients are computed with respect to the vertical and correspond to the equivalent VTI model that describes wave propagation in the symmetry-axis plane. A more intuitive form of Ruger's approximation is:

$$R(i,\phi) = A + B(\phi)\sin^2 i + C(\phi)\sin^2 i \tan^2 i \tag{2.29}$$

The term A is the normal-incidence reflection coefficient. The term $B(\phi)$ is so-called AVO gradient which can be written as:

$$B(\phi) = B_{iso} + B_{ani}\cos^2(\phi - \phi_{sym}) \tag{2.30}$$

The symmetry axis forms an angle ϕ_{sym} with the x-axis. The term B_{iso} is the AVO-gradient isotropic part (equal to the AVO gradient for isotropic media), and B_{ani} is the anisotropic part of AVO gradient:

$$B_{iso} = \frac{1}{2}\left[\frac{\Delta\alpha}{\alpha} - \left(\frac{2\overline{\beta}}{\overline{\alpha}}\right)^2 \frac{\Delta G}{\overline{G}}\right], \tag{2.31}$$

and

$$B_{ani} = \frac{1}{2}\left[\Delta\delta^v + 2\left(\frac{2\overline{\beta}}{\overline{\alpha}}\right)\Delta\gamma\right]. \tag{2.32}$$

The shape of the variation of AVO gradients with azimuth is determined by both B_{iso} and B_{ani} (Rüger, 1996). A parallel direction to the fractures corresponds to only B_{iso}, while a perpendicular direction corresponds to $B_{iso} + B_{ani}$.

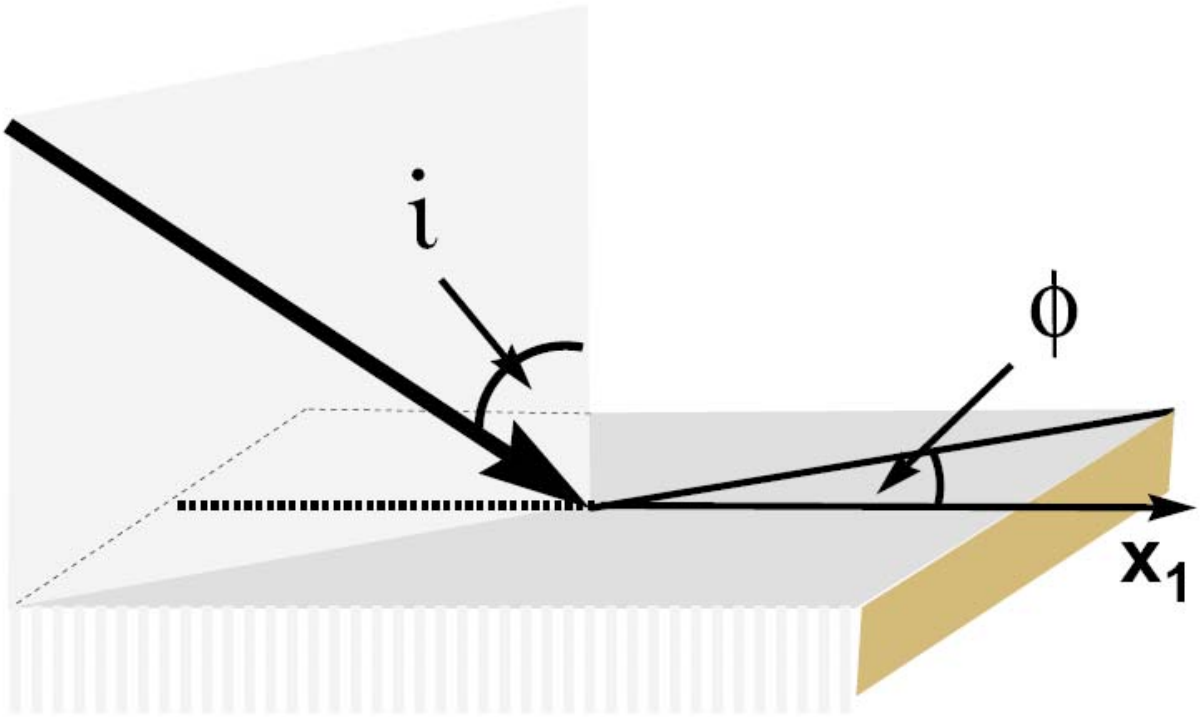

Figure 2.9 Reflection response for vertically fractured reservoir (HTI media) as a function of incidence angle *i* and azimuth ϕ (after Rüger, 1996).

2.3 Summary

Understanding the basic principles of subjects covered in this chapter was important for the research topic. The first part discussed seismic anisotropy, its definition, importance, causes and symmetry classes. Transverse isotropy (TI), the simplest type of symmetry classes, was discussed in more details since analyses in this research are done on a TI model. The second part of this chapter gave a background on how the story of seismic partitioning of energy at an interface started and evolved over the years. The importance of amplitude variation with offset in quantifying medium parameters was highlighted. Both isotropic and anisotropic AVO equations were covered.

CHAPTER 3
LABORATORY EXPERIMENTS

3.1 Introduction

Seismic wave propagation and partitioning of energy at an interface can be effectively studied by using physical modelling, whereby models are constructed in such a way that they resemble real geological structures taking into account the distance scale factor. Hence, by using scaled models in a controlled environment, it can be assumed that the response from the models is the same as it would have been obtained from realistic earth materials.

An advantage of laboratory experiments is that real seismic waves propagate through models with no approximations made to the propagation process. On the other hand, physical modelling is prone to technical problems and errors which will be discussed later in this chapter.

Typical problems encountered in physical modelling are:

1. The availability of materials with specific velocities (P- and S-wave).
2. Type and dominant frequency of transducers can be limited.
3. Source and receivers have to be accurately positioned which is limited by the available technology.
4. Unwanted interfering events can hinder useful seismic events.

In this project I used physical modelling to measure amplitude variation with offset for isotropic and anisotropic models and compared the results to numerical simulations. Transmission measurements were performed in order construct the elasticity tensor for an HTI model. This elasticity tensor was then used as an input into numerical simulations. Two reflection measurements were performed; the first one was for a water/isotropic Plexiglas interface and the second one was for a water/anisotropic (HTI) interface at different azimuths. Both transmission and reflection experiments are discussed in more detail.

3.2 Physical laboratory and equipment

Laboratory experiments were conducted using the Curtin University Physical Modelling Laboratory equipment (Figure 3.1 a) (Luo and Evans, 2004). The system comprises a set of computer controlled ultrasonic piezoelectric transducers, operating as seismic source and receivers. Movement of transducers is controlled in three-dimensions by high-precision stepping motors. A Lab View data acquisition program enables versatile source-receiver configurations, which can be transmission measurements, or reflection 2-D, 3-D and VSP surveys.

A source generator can be used to generate an electronic pulse and excite the transducer to create the ultrasonic source wavelet. These ultrasonic pulses are detected by the receiving transducer where the signal is converted back to an electric signal. This signal is then amplified using a receiver amplifier (Panametrics, 1987). The A/D converter then converts the signal from analogue to digital format and output data as binary, SU or SEGY format file (Figures 3.1 b, c).

Transducers are used in physical modelling experiments as seismic sources and/or receivers. They contain piezoelectric material that generates mechanical energy (ultrasonic waves) when placed in an electric field. At the same time they convert mechanical (wave energy) into electrical signals. Depending on their radiation pattern, transducers can be categorized as two main types:

- Directional transducers which are typically used for transmission measurements.
- Omni-directional transducers which radiate energy equally in all directions. For this reason, they are suitable for AVO analysis.

Transducers are also categorized according to their source type. They can be P-wave or S-wave transducers and they come with different dominant frequencies. It is preferable to excite transducers with their resonant frequency for optimum S/N ratio. For P-wave recording (transmission and reflection), omni-directional cylindrical wave transducers

(a)

(b) **(c)**

Figure 3.1 (a) Physical modelling system at Curtin University. A PC controls the seismic source and receivers in an x, y and z coordinate system, (b) is a source generator, and (c) is an analogue to digital converter.

were used which posses a dominant frequency of 220 kHz. 500 kHz directional transducers were used for S-wave recording. Both P- and S-wave transducers used are shown in Figures 3.2 a, b.

3.3 Construction of the physical model

Physical properties of model materials need to be considered carefully to ensure successfully built physical models. For solid media this includes P and S-wave velocities and density. Plexiglas is often a material of choice since it is intrinsically isotropic but at the same time can be cast in very fine layers which can be pressed together to simulate a fractured (anisotropic) medium. Plexiglas has a P-wave velocity of about 2700 m/s which provides a good velocity contrast with a water column. Its density of 1.2 g/cc allows the material to be positioned deep into a water tank.

The objective of the laboratory experiments was to analyse the variations of P-wave reflectivity with incidence angle and azimuth caused by a set of vertical fractures embedded into an otherwise isotropic medium. Thin Plexiglas plates (2mm thick) were used to construct the fractured model. The surfaces of the Plexiglas sheets were roughened to establish asperities. Then the plates were pressed together under water to make sure that no air bubbles were trapped inside. With a scaling factor of 1:10000, the model simulated a 500 m thick fractured medium, with 20 m fracture separation, over an area of 1500 × 1200 m. A solid block of Plexiglas of the same dimensions was used for calibration. Physical models are show in Figures 3.3 a, b.

3.4 Transmission measurements

Transmission measurement of P- and S-waves through a fractured model is an effective tool in quantifying model's fracture-induced seismic anisotropy. The first step after designing the desired HTI model is to check that it shows expected anisotropy (Urosevic, 1985). Transmission measurements were performed to construct the elasticity tensor of both the solid and the fractured model. These elasticity tensors were used as an input into numerical simulations, quantification of fracture-induced seismic anisotropy and accordingly the extraction of anisotropic parameters from transmission measurements,

(a)

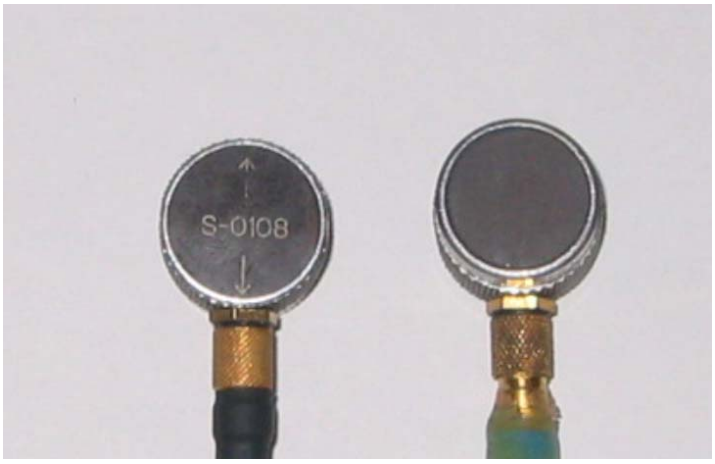

(b)

Figure 3.2 (a) Omni-directional P-wave cylindrical transducers with 220 kHz dominant frequency. (b) Directional S-wave transducers with 500 kHz dominant frequency (active elements of transducers are 8mm and 6mm in diameter, respectively).

(a)

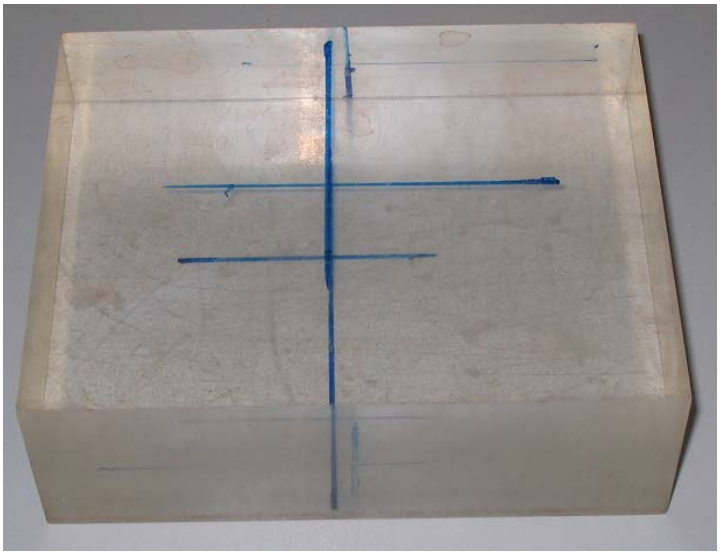

(b)

Figure 3.3 (a) Fractured model with 2mm Plexiglas plates. (b) Solid block used for calibration.

made it possible for direct comparison between laboratory measurement and numerical simulations.

3.4.1 Transmission measurements through isotropic Plexiglas model

The solid block of Plexiglas was assumed to be isotropic because it generally has neither impurities nor intrusions. For that reason, only two velocity measurements were needed (P- and S-wave) to construct its stiffness matrix. Measurement can be taken at any direction since the velocity is the same at all directions for the isotropic case.

A pair of omni-directional P-wave transducers with a dominant frequency of 220 KHz was used for P-wave velocity measurements. One transducer was used as a source and the other as a receiver. In order to get as accurate value of travel time as possible, one transducer was fixed touching the model from one side (source transducer) and the other (receiver transducer) moved along the other side from one edge to the other as shown in Figure 3.4 a.

The shortest travel time represented the position when both transducers were exactly aligned. The common shot gather is shown in Figure 3.4 b. P-waves propagated though the isotropic block with a velocity of 2724 m/s. For S-wave velocity, a pair of S-wave transducers with a dominant frequency of 500 kHz was used. The measured S-wave velocity was 1384 m/s. The water velocity was also measured (1484 m/s) to ensure accurate numerical simulations.

“Cylindrical transducers have a radiation pattern which is circular viewed from the end of the transducer. There is an additional but very minor radiation lobe out of each end of the transducer but in principle all of the power is radiated equally at all angles orthogonal to the radiating surface, irrespective of angle.”

"The accuracy of travel times is entirely a function of sample rate. If the sample rate were 0.1 microseconds, then the accuracy of the travel time pick should be no more than 2% of this or +/- 2 nanoseconds." (B. Evans, Pers. Comm., 2007).

3.4.2 Transmission measurements through the fractured model

Five velocity measurements are needed for the extraction of five elastic parameters which fully describe the TI media (Mavko, 1998): $V_p(0^o), V_p(90^o), V_p(45^o), V_{sh}(90^o)$, and $V_{sh}(0^o) = V_{sv}(0^o)$ where, $V_p(0^o)$ is P-wave velocity at zero degrees to the axis of symmetry (the velocity of P-wave which propagates perpendicular to the fractures).

$V_p(90^o)$ is the P-wave velocity that propagates along the fractures or 90 degrees to the axis of symmetry. $V_p(45^o)$ is the P-wave velocity at 45 degrees to the symmetry axis (Figures 3.5 a, b and c). The $V_{sh}(0^o)$ and $V_{sv}(0^o)$ are *S*-wave velocities polarized within the isotropy plane while propagating perpendicular to fractures (0 degrees to the axis of symmetry). $V_{sh}(90^o)$ is the S-wave velocity polarized within the symmetry plane while propagating parallel to fractures (90 degrees to the axis of symmetry). It is more convenient to denote *S*-wave velocities as fast and slow waves or S-wave parallel ($S^{\parallel}$) and S-wave perpendicular ($S^{\perp}$) with respect to the fracture direction. The difference between the two is called S-wave birefringence.

One constraint that was faced during S-wave measurement is recovering the velocity values of $V_{sh}(0^o)$ and $V_{sv}(0^o)$ because there was no signal when transducers were put at 0 degrees (across the fractures) to the axis of symmetry. But these values could be obtained by the setting $V_{sh}(0^o) = V_{sv}(90^o)$.

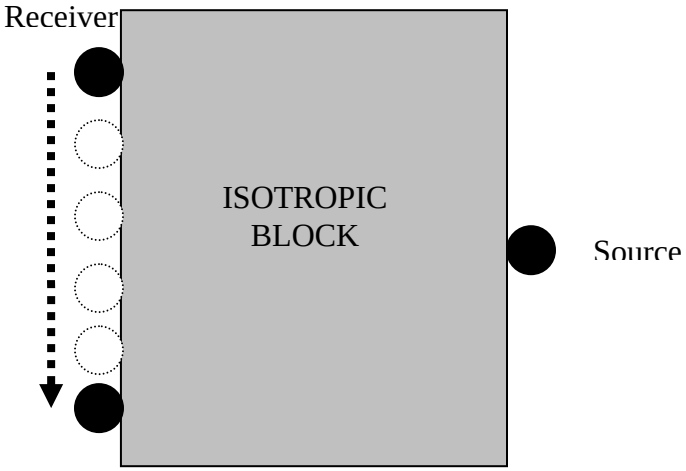

(a)

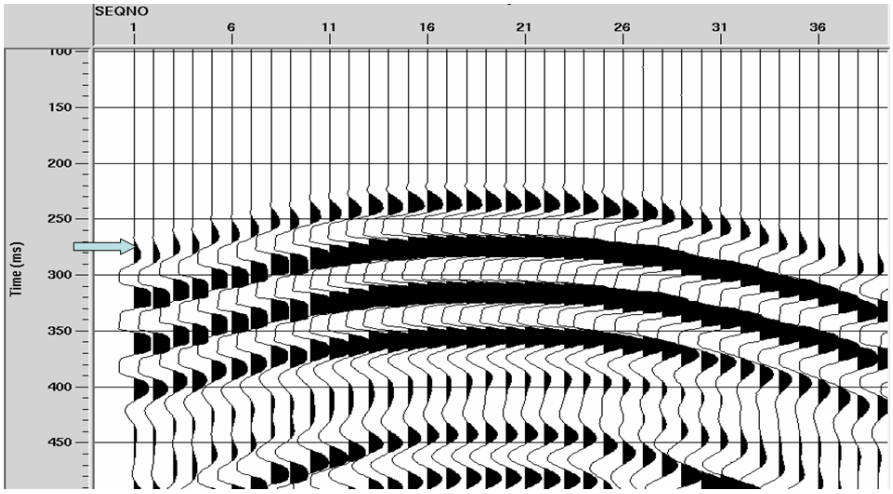

(b)

Figure 3.4 (a) Transmission measurement scheme where one transducer was fixed touching the model from one side (source transducer) and the other (receiver transducer) moved along the other side from one edge to the other. (b) The resulting shot gather.

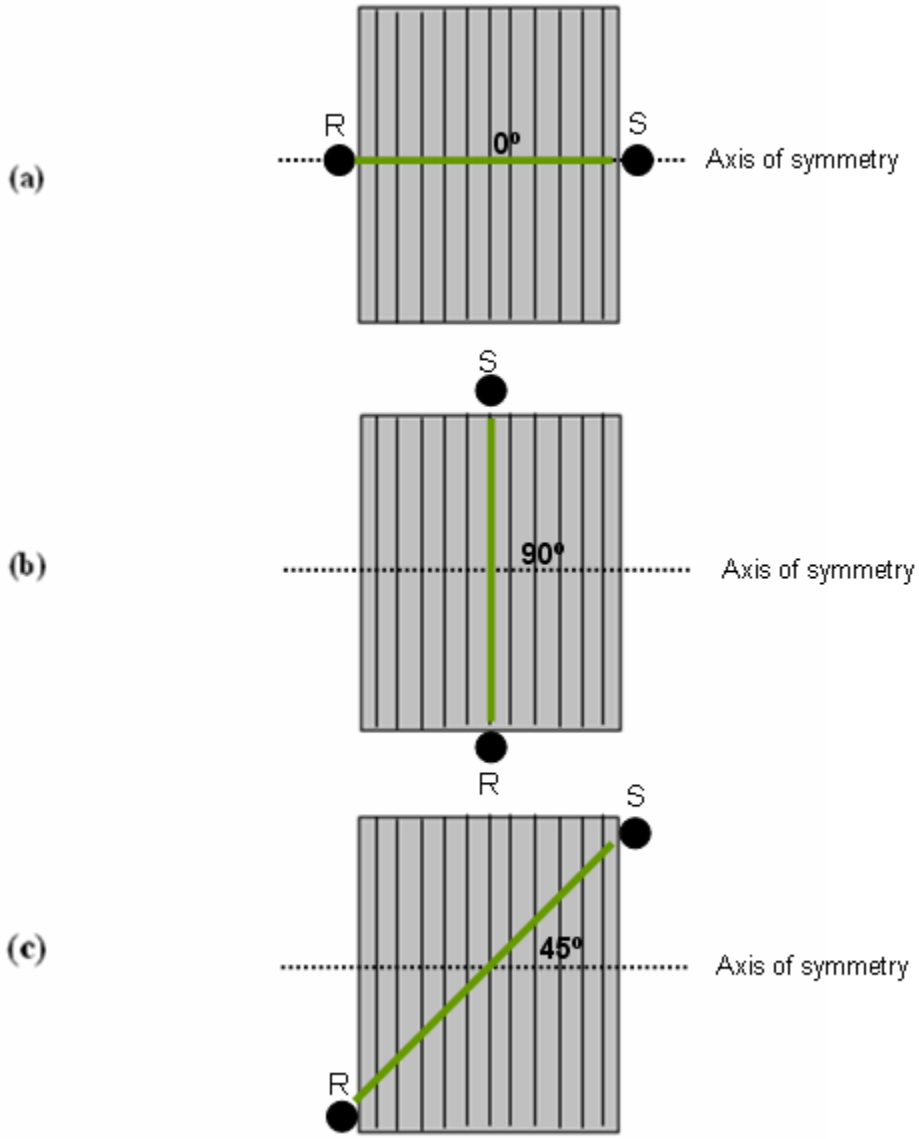

Figure 3.5 Trasmission measurements at 0, 90 and 45 degrees with respect to the axis of symmetry.

The brackets holding the Plexiglas plates together hindered direct measurement of $V_p(45^o)$ and alternatively it was estimated from HTI elastic constants using this relation (Mavko, 1998):

$$C_{13} = -C_{44} + \sqrt{4\rho^2 V_{P(45°)}{}^4 - 2\rho V_{P(45°)}{}^2 (C_{11} + C_{33} + 2C_{44}) + (C_{11} + C_{44})(C_{33} + C_{44})} \qquad (3.1)$$

To estimate C_{13} elastic constant (described in more detail in the next chapter) offset transmission experiments were needed. These measurements involved a fixed source transducer and a moveable receiver transducer. This acquisition configuration is similar to that of a walk-way VSP survey. The acquisition scheme is shown in Figure 3.6.

Transmission velocity values for the solid model, the fractured model, and water along with their densities are shown in Table 3.1.

Solid Model	V_P	V_S	ρ	Water	V_P	ρ
	2.724	1.384	1.2		1.484	1
Fractured Model	$V_P(0)$	$V_P(45)$	$V_P(90)$	$V_s(fast)$	$V_s(slow)$	ρ
	2.704	2.660	2.709	1.382	1.320	1.2

Table 3.1 Elastic parameters of the solid (isotropic) and the fractured (anisotropic) Plexiglas models. Velocities are in km/s and densities in g/cc.

3.5 Reflection measurements

The goal of this experiment was to record a multi-azimuthal AVO reflection survey over a fractured model with known anisotropic parameters calculated from transmission measurements. The results were then analysed and compared to numerical modelling in order to study the effect of fracture-induced anisotropy on the AVO reflection response and therefore infer the model's fracture parameters.

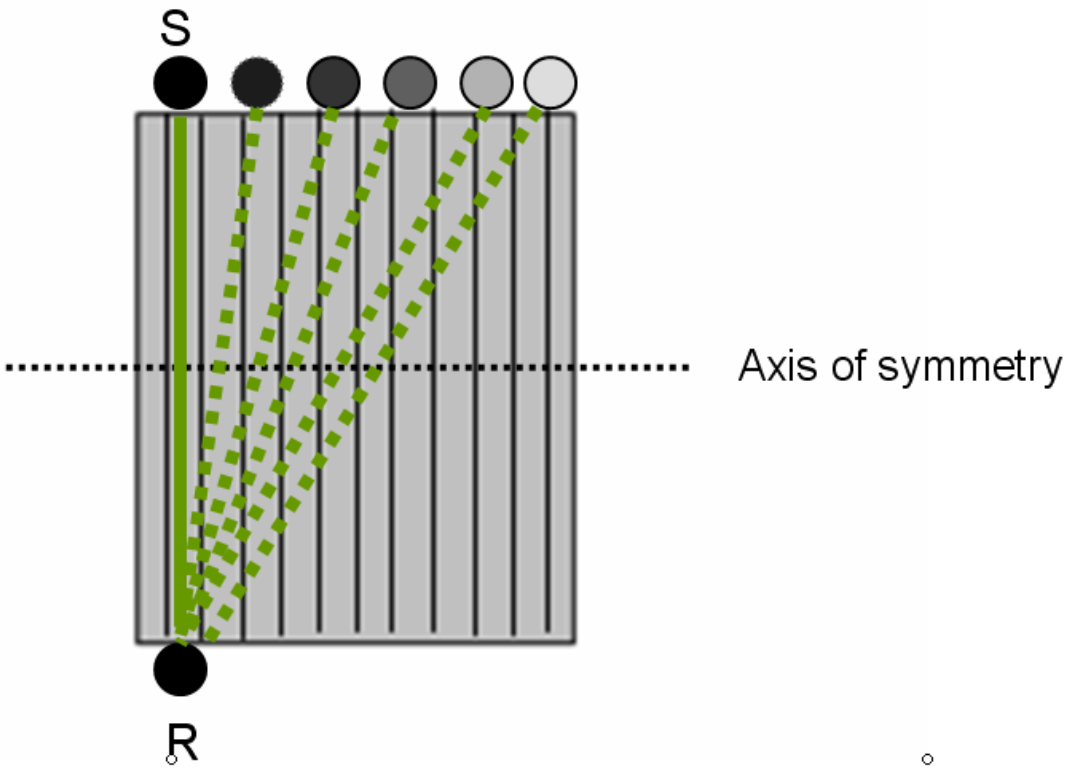

Figure 3.6 Side view of offset transmission measurement. The source was stationary while the receiver moved from one side of the model to the other.

3.5.1 Isotropic reflection experiment

The first reflection experiment was performed with a water/solid Plexiglas interface. The recorded AVO response was used for calibration and to compare the radiation pattern of transducers with numerical modelling.

The solid block of Plexiglas was submerged in a water tank. Omni-directional P-wave transducers with a 220 kHz dominant frequency were also submerged in water and positioned 24 cm (2.4 km, scaled) above the model. Common mid-point (CMP) recording was employed for data acquisition. The minimum offset was 2 cm and source and receivers were moved apart at an increment of 1 mm in the opposite directions. A total of 270 CMP traces were recorded over the model. At each position, 20 CMP traces were repeated and vertically stacked to increase the signal-to-noise ratio. With a length scaling factor of 1:10000, this model simulated 20 m trace spacing, and a dominant source wavelet of 22 Hz reflecting from an interface at a depth of 2.4 km. The acquisition parameters and the resulting CMP gather are shown in Figures 3.7 a, b.

3.5.2 AVOaz experiment

For AVOaz reflection experiments, all acquisition parameters were kept the same as in the previous experiment over the isotropic model, but instead of recording a single 2-D CMP line, a total of seven 2-D lines were recorded along different azimuths with the middle CMP being at the centre of the fractured model. The azimuths were measured with respect to the symmetry axis direction, starting from zero azimuth (perpendicular to fractures) up to 90 degrees azimuth (parallel to fractures) with an increment of 15 degrees. For every 2-D CMP line, the model was rotated 15 degrees with respect to the symmetry axis. Figure 3.8 illustrates three azimuthal recordings at 0, 45 and 90 degrees. The black dotted line is the symmetry axis and the red lines are the 2-D CMP lines corresponding to three azimuthal directions.

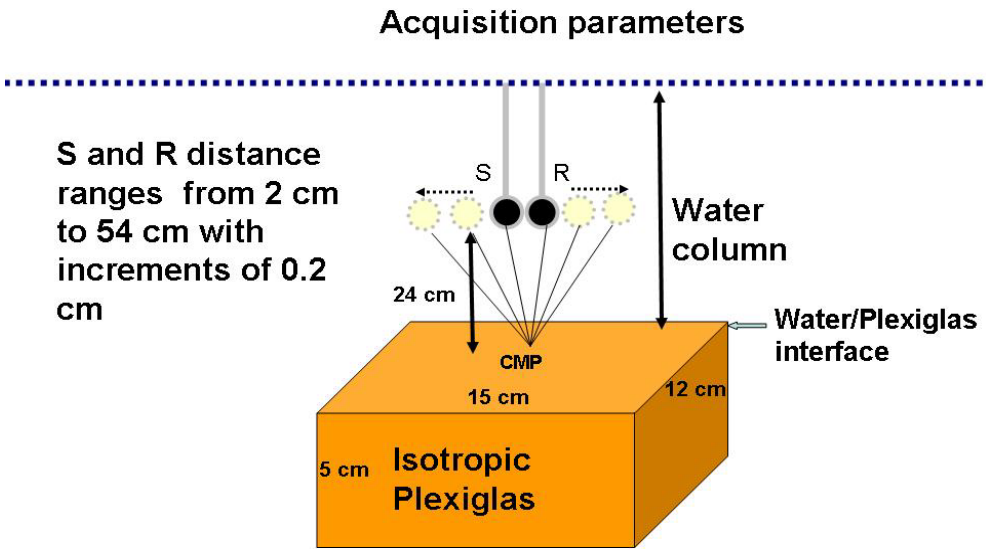

(a)

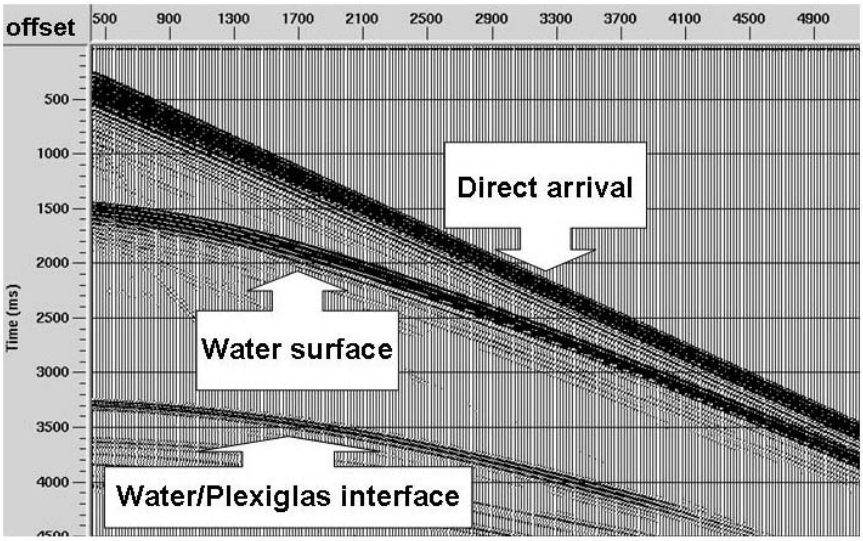

(b)

Figure 3.7 (a) Acquisition parameters of the reflection measurement for water/Plexiglas interface producing CMP gathers (b) with three seismic events indicated by arrows.

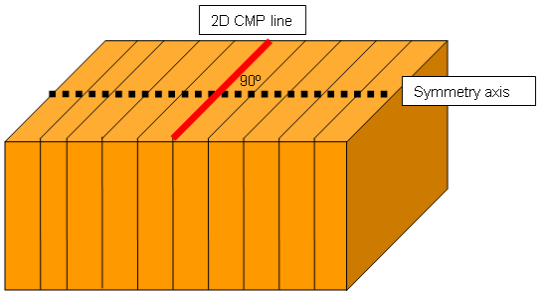

(a)

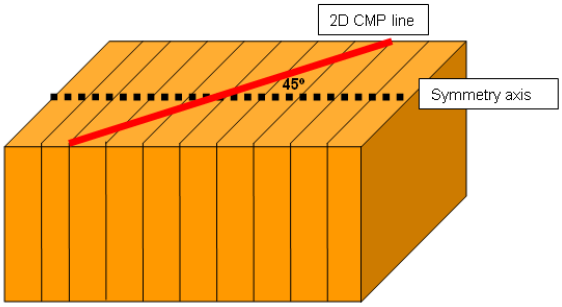

(b)

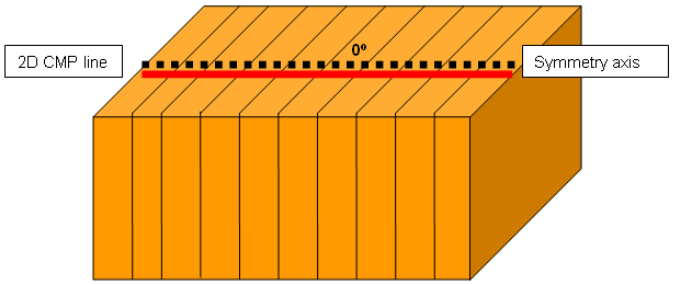

(c)

Figure 3.8 Three azimuthal recordings at 0, 45 and 90 degrees with respect to the symmetry axis.

3.6 Physical experiments difficulties

Constructing the right models and running laboratory experiments with a high level of quality was not an easy task. A lot of issues had to be considered as early as how to initially construct the physical model. For this research, a fractured model was meant to be simulated and in order to measure anisotropy, the wavelet had to be large enough compared to fracture's separation. For this reason, it was important to use transducers with a dominant frequency low enough to meet the theory of effective medium.

Plexiglas is an excellent physical modelling material and the thinnest sheets I could find were 2 mm thick. At the beginning I intended to use a 50 kHz spherical transducer where the wavelet was calculated to be 27 times the fracture's separation. Unfortunately it was very difficult to deal with low frequency transducers, where vertical resolution and separation of seismic events was problematic. As an alternative solution, I used omni-directional cylindrical transducers having a dominant frequency of 220 kHz, which reduced the wavelet to six times the fracture's separation

Delays in P- and S-wave transducers were accounted for which would have resulted in incorrect velocity values. The delays were 41 and 15 microseconds for P- and S-wave transducers respectively (Figure 3.9 a, b), due to their relative distances from the cryptal to the transducers outer layer. To calculate the correct velocity, we first picked the first break time. After that we subtracted transducer's delay time for it. Finally, the velocity is computed from the new time and the transducer's separation distance. The sample rate of 0.1 μs ensures accurate traveltime reading. Vertical stacking was used (20 fold) as a tool to increase signal-to-noise ratio to get accurate first break picking.

There was a construction problem with the fractured model where the two clamps used to hold the Plexiglas plates together resulted in a weak area in the middle section of the model and the stress was not evenly distributed throughout the fractures. This affected the transmission measurement and resulted in incorrect extraction of anisotropic parameters. The problem was solved by putting another clamp in the middle section of the model and re-measuring transmission values (Figures 3.10 a, b).

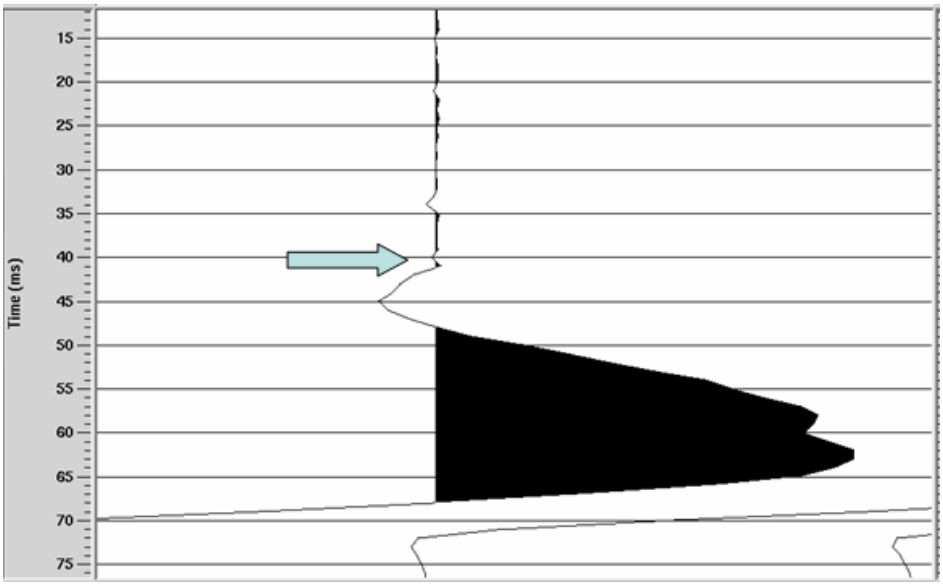

(a)

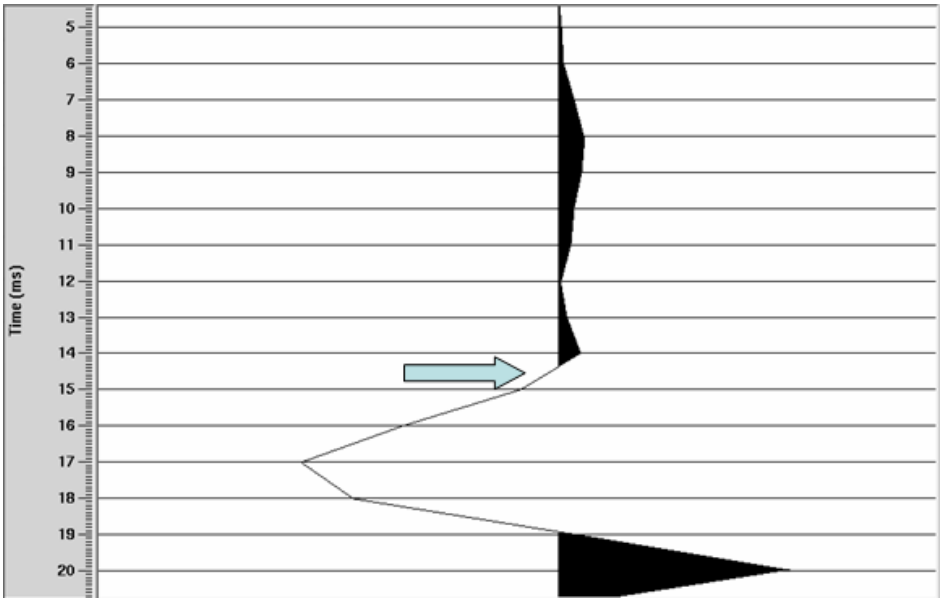

(b)

Figure 3.9 Delays in P-wave (a) and S-wave (b) transducers indicated by arrows. These delays were a result of the distance of the transducers crystal to the transducers outside layer.

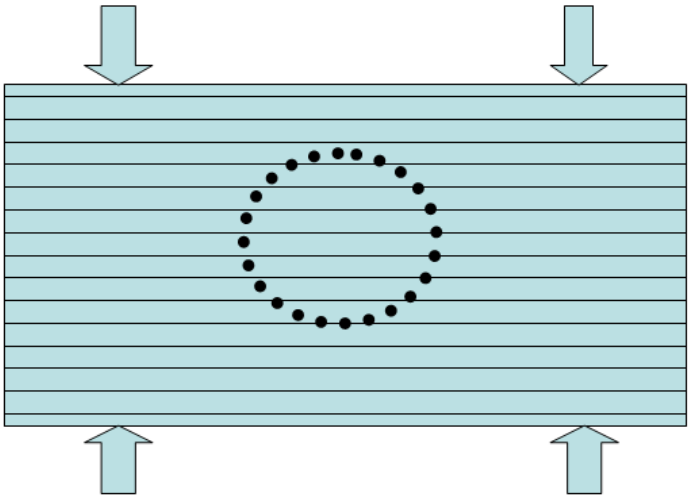

(a)

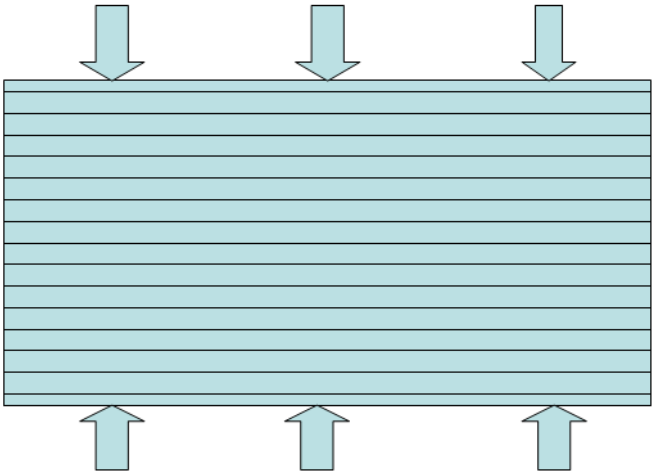

(b)

Figure 3.10 (a) The HTI model with two clamps used to hold the Plexiglas together caused uneven distribution of stress thoughout the model which resulted in a weak zone in the middle section (indicated by the circle). (b) The HTI model after adding another clamp in the middle section had more even stress distribution.

CHAPTER 4
THE EXTRACTION OF ELASTIC CONSTANTS AND ANISOTROPIC PARAMETERS

4.1 The extraction of elastic constants

The elastic constants of both the isotropic (solid Plexiglas) and the anisotropic (Fractured) models were extracted using transmission measurement results (Table 3.1). These elastic constants were used to construct the stiffness matrices of both media.

Only two independent constants are needed to fully describe the isotropic medium. The following relations were used to calculate the stiffness matrix of isotropic material (Mavko et al., 1998):

$$C_{11} = V_P{}^2 \rho, \tag{4.1}$$

$$C_{44} = V_S{}^2 \rho, \tag{4.2}$$

$$C_{12} = C_{11} - 2C_{44}, \tag{4.3}$$

where ρ is the density of Plexiglas (1.2 g/cc). V_P and V_S are measured P and S-wave velocities through the homogeneous isotropic Plexiglas model (V_P = 2724 m/s and V_S =1384 m/s). The resultant isotropic stiffness matrix has the form:

$$C_{ij=}\begin{bmatrix} 8.904 & 4.307 & 4.307 & 0 & 0 & 0 \\ 4.307 & 8.904 & 4.307 & 0 & 0 & 0 \\ 4.307 & 4.307 & 8.904 & 0 & 0 & 0 \\ 0 & 0 & 0 & 2.2985 & 0 & 0 \\ 0 & 0 & 0 & 0 & 2.2985 & 0 \\ 0 & 0 & 0 & 0 & 0 & 2.2985 \end{bmatrix}. \tag{4.4}$$

Five independent elastic constants are required to fully describe an HTI medium. These elastic constants are related to velocity measurements and densities by these relations (Mavko, 1998):

$$C_{11} = \rho V_P{}^2(90°), \tag{4.5}$$

$$C_{12} = C_{11} - 2\rho V_{SH}{}^2(90°), \tag{4.6}$$

$$C_{33} = \rho V_P{}^2(0°), \tag{4.7}$$

$$C_{44} = \rho V_{SH}{}^2(0°), \tag{4.8}$$

$$C_{66} = \frac{1}{2}(C_{11} - C_{12}). \tag{4.9}$$

$V_{SH}(0°)$ value could not be obtained from transmission measurements since there was no signal for S-wave propagating across the fractures (0º to the axis of symmetry). The problem was over come by using the equation for a quasi-shear mode. The equation for a quasi-shear mode is written as (Mavko, 1998):

$$V_{SV} = \left[C_{11}\sin^2\theta + C_{33}\cos^2\theta + C_{44} - (\sqrt{M})\right]^{1/2}(2\rho)^{-1/2}, \tag{4.10}$$

where

$$M = \left[(C_{11} - C_{44})\sin^2\theta - (C_{33} - C_{44})\cos^2\theta\right]^2 + (C_{13} + C_{44})^2\sin^2 2\theta, \tag{4.11}$$

θ is the angle between the wave vector and the axis of symmetry. At $\theta = 90°$,

$$M = (C_{11} - C_{44})^2, \tag{4.12}$$

By substituting the value of the M in equation (4.11) with $V_{SV}(90°)$ we get

$$C_{44} = \rho V_{sv}{}^2(90°). \tag{4.13}$$

The elastic constant C_{13} was accurately estimated by using transmission velocity values obtained from the offset transmission experiment discussed in Chapter 3.4.2. C_{13} was obtained by the least square fitting of the measured angular velocity data using fixed predetermined values of C_{11}, C_{33}, C_{44} and C_{66} (Fatkhan, 2003). In other words C_{13} was estimated by minimizing the differences between the computed theoretical, and the observed P- and S-wave arrival time for all incidence angles. A Matlab code which utilizes a Graphic User Interface (GUI) and which enables interactive estimate of the C_{13} parameter was written for this purpose (Fatkhan, 2003).

Figure 4.1 illustrates the agreement between the measured transmission values for the offset experiment (described in Figure 3.6) and theoretical velocities for the HTI model, through the process of the least square fitting.

All mathematical relations used to derive the five elastic constant are written for vertical transverse isotropic medium (VTI medium) and the resulting elastic constants are in VTI notation. The values are as follow:

C_{11} = 8.8064, C_{33} = 8.7869, C_{13} =4.0, C_{12} = 4.2226 C_{44} =2.0909 and C_{66} = 2.2919. The unit is GPa. Correspondingly, the stiffness matrix of the VTI medium is:

$$C^{(VTI)}_{ij=}\begin{bmatrix} 8.806 & 4.223 & 4.0 & 0 & 0 & 0 \\ 4.223 & 8.806 & 4.0 & 0 & 0 & 0 \\ 4.0 & 4.0 & 8.787 & 0 & 0 & 0 \\ 0 & 0 & 0 & 2.0909 & 0 & 0 \\ 0 & 0 & 0 & 0 & 2.0909 & 0 \\ 0 & 0 & 0 & 0 & 0 & 2.2919 \end{bmatrix}. \qquad (4.14)$$

The symmetry axis of VTI media is vertical (coincides with the x_3-axis) as shown in Figure 4.2 a. and tilting the symmetry axis all the way to horizontal will give HTI media where the symmetry direction coincides with the x_1-axis (Figre 4.2 b). As a result of this analogy between the VTI and HTI media, the stiffness tensor of the HTI media can be obtained from that of the VTI model by interchanging the indices 1 and 3 (Tsvankin, 2001).

Using the matrix notation (Voigt recipe), we find the following transformation rule for the non-zero stiffness components responsible for wave propagation in the (x_1-x_2)-plane (Tsvankin, 2001):

$C_{11} = C^{(R)}{}_{33}$; $C_{33} = C^{(R)}{}_{11}$; $C_{13} = C^{(R)}{}_{13}$; $C_{55} = C^{(R)}{}_{55}$; $C_{44} = C^{(R)}{}_{66}$; $C_{66} = C^{(R)}{}_{44}$

The superscript R indicates the vertical rotation of stiffnesses and the resulting HTI elastic parameters are as follow:

$C_{11} = 8.7869, C_{33} = 8.8064,\ C_{13} = 4.0,\ C_{44} = 2.2919$ and $C_{55} = 2.09088$

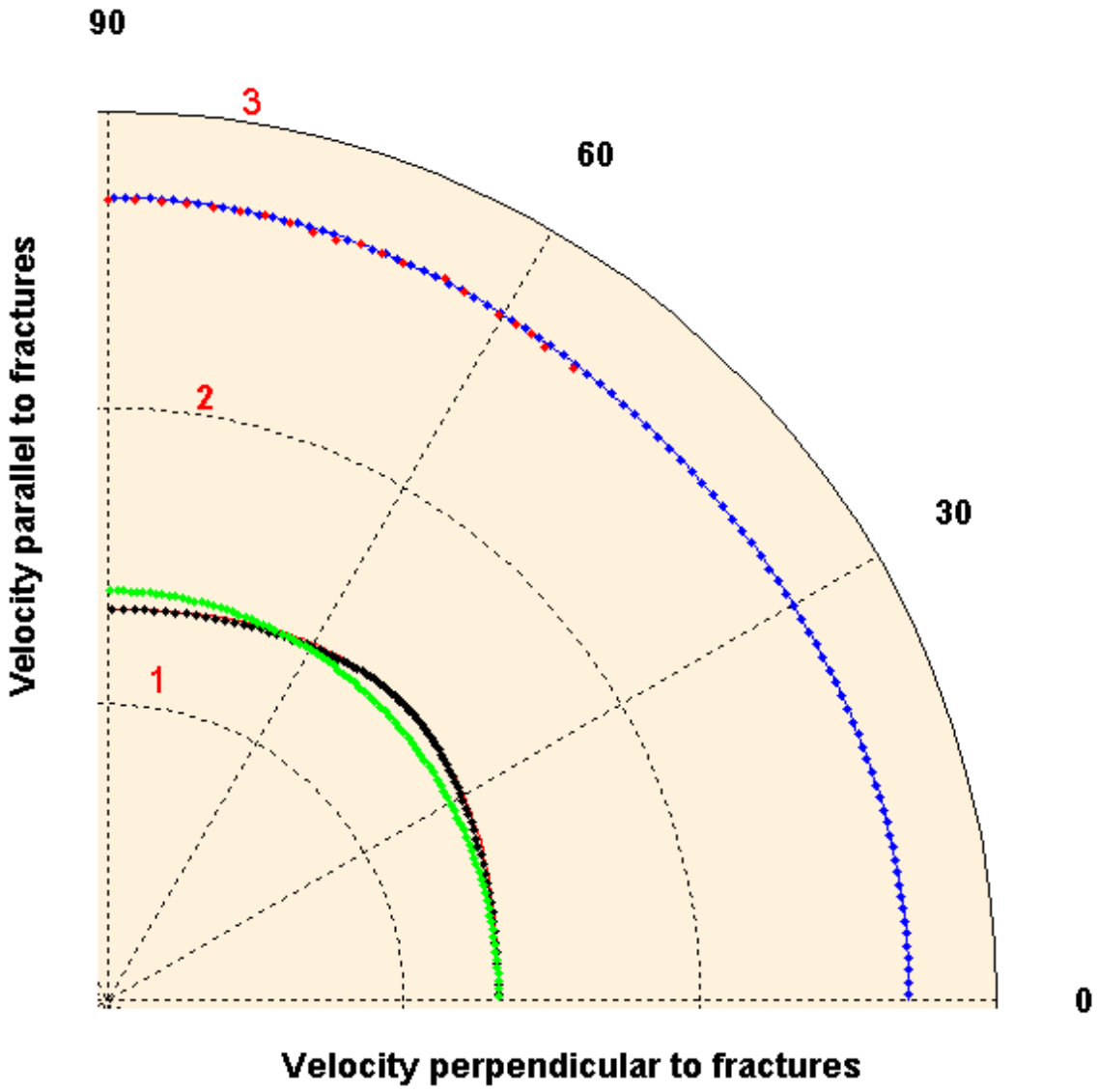

Figure 4.1 The agreement between the measured and theoretical velocities for the HTI model, through the process of the least square fitting. The red dots are the measured velocities and the blue dots are the computed velocities. The black and green lines are SV and SH velocities.

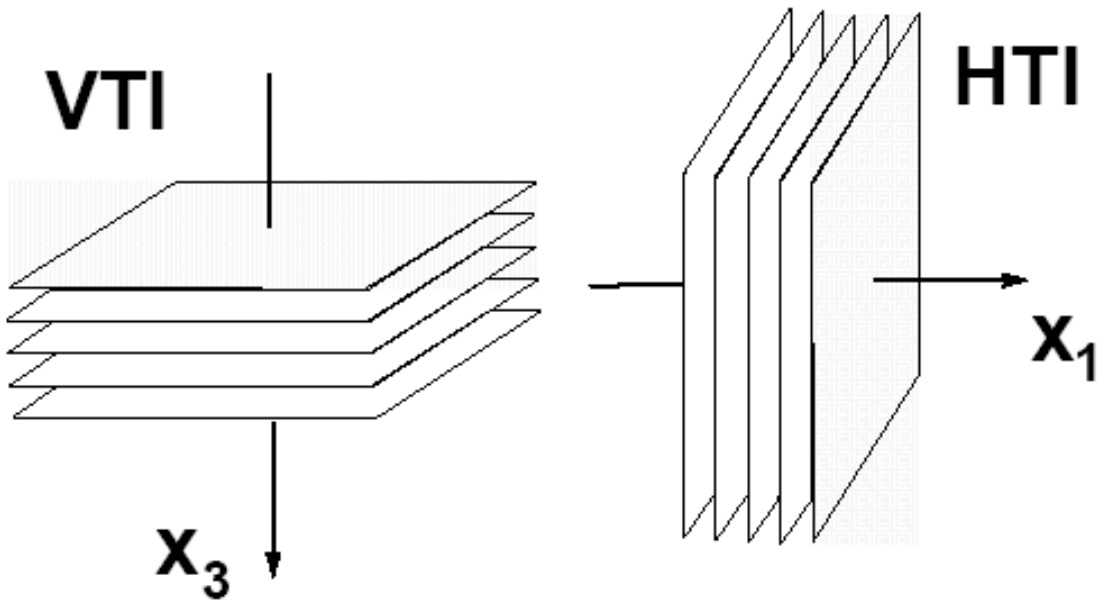

(a) (b)

Figure 4.2 The analogy between VTI media (the symmetry direction coincides with x_3-axis) (a) and HTI media (the symmetry direction coincides with x_{-1} axis) (b) (Rüger, 2001).

The HTI stiffness matrix can then be written in term of elastic parameters as:

$$C^{(HTI)}_{ij=}\begin{bmatrix} 8.787 & 4.0 & 4.0 & 0 & 0 & 0 \\ 4.0 & 8.806 & 4.22 & 0 & 0 & 0 \\ 4.0 & 4.22 & 8.806 & 0 & 0 & 0 \\ 0 & 0 & 0 & 2.2919 & 0 & 0 \\ 0 & 0 & 0 & 0 & 2.0909 & 0 \\ 0 & 0 & 0 & 0 & 0 & 2.0909 \end{bmatrix}. \tag{4.15}$$

4.2 The extraction of anisotropic parameters

Elastic constants recovered from the physical models were subsequently used to compute Thomsen's (1986) anisotropy parameters. The generic Thomsen parameters ε, γ and δ

$$\varepsilon = \frac{C_{11} - C_{33}}{2C_{33}}, \tag{4.16}$$

$$\gamma = \frac{C_{66} - C_{44}}{2C_{44}}, \tag{4.17}$$

$$\delta = \frac{(C_{13} - C_{44})^2 - (C_{33} - C_{44})^2}{2C_{33}(C_{33} - C_{44})}. \tag{4.18}$$

The resulting anisotropic parameters are $\varepsilon = 0.0011$, $\gamma = 0.0481$ and $\delta =$ -0.0658.

Rüger (1996) introduced a new form of Thomsen parameters inverted for HTI media and denoted by (*v*) which means that they are defined with respect to the vertical symmetry axis. The new anisotropic parameters ε^v, γ^v and δ^v can be expressed though the generic Thomsen parameters ε, γ and δ using these relations (Ruger, 1996):

$$\varepsilon^v = \frac{-\varepsilon}{1+2\varepsilon}, \tag{4.19}$$

$$\gamma^{V} = \frac{-\gamma}{1+2\gamma}, \tag{4.20}$$

$$\delta^{V} = \frac{\delta - 2\varepsilon(1+\frac{\varepsilon}{f})}{(1+2\varepsilon)(1+\frac{2\varepsilon}{f})}, \tag{4.21}$$

where $f = 1-(V_{S0}/V_{P0})^2$ and both V_{S0} and V_{P0} are measured along the horizontal symmetry axis. The resulting values are ε^{V} = -0.0011, γ^{V} = -.044 and δ^{V} = -.068.

A summary of all extracted elastic constants for isotropic and anisotropic models and corresponding anisotropic parameters in both VTI and HTI notations are listed in Tables 4.1 and 4.2.

Isotropic Elastic constants	**C11**	**C12**	**C44**		
	8.904	4.307	2.2985		
Elastic constants (VTI notation)	**C11**	**C33**	**C13**	**C44**	**C66**
	8.8064	8.7869	4.0	2.0909	2.2919
Elastic constants (HTI notation)	**C11**	**C33**	**C13**	**C44**	**C55**
	8.7869	8.8064	4.0	2.2919	2.0909

Table 4.1 Elastic constants for both isotropic and anisotropic models.

Anisotropic parameters in VTI notation	ε	γ	δ
	0.0011	0.0481	-0.0658
Anisotropic parameters in HTI notation	ε^{v}	γ^{v}	δ^{v}
	-0.0011	-0.044	-0.068

Table 4.2 Anisotropic parameters of fractured model in VTI and HTI notations.

CHAPTER 5
SPHERICAL WAVE EFFECT ON AVO RESPONSE IN ISOTROPIC MEDIA AND IMPLICATIOS FOR THREE-TERM INVERSION

5.1 Introduction

In this chapter the spherical wave effect on the AVO response is verified by comparing the experimental results (Chapter 3) to full-wave numerical simulations. I show how spherical AVO response changes with frequency and how it can cause wrong parameter extraction. A more robust methodology for three-parameter inversion is suggested.

5.2 Numerical simulations and comparison

In order to obtain water/Plexiglas reflection coefficients R_{PP} from the gathers of Figure 3.7b, the amplitudes of the water/Plexiglas reflection were picked, corrected for geometrical spreading, and calibrated at near offset to the theoretical zero-offset reflection coefficient. The resulting R_{PP} values are plotted in Figure 5.1 as a function of incidence angle θ. Also shown in Figure 5.1 are theoretical plane-wave (Zoeppritz) reflection coefficients computed from elastic parameters extracted from transmission measurements. The plane wave solution agrees very well with the physical modeling data for moderate angles of incidence (up to 20º). On the other hand, there is a big discrepancy at large angles, especially those close to the critical angle. This discrepancy is most likely caused by spherical wave effects (Krail and Brysk, 1983; Haase, 2004; Doruelo et al., 2006; and Van der Baan and Smit, 2006).

In order to take into account the spherical wave effects, the amplitude versus incidence angle (AVA) response was simulated using a full-wave reflectivity algorithm with a point source. The resulting amplitudes were picked on seismograms and corrected for geometrical spreading are also shown in Figures 5.1.

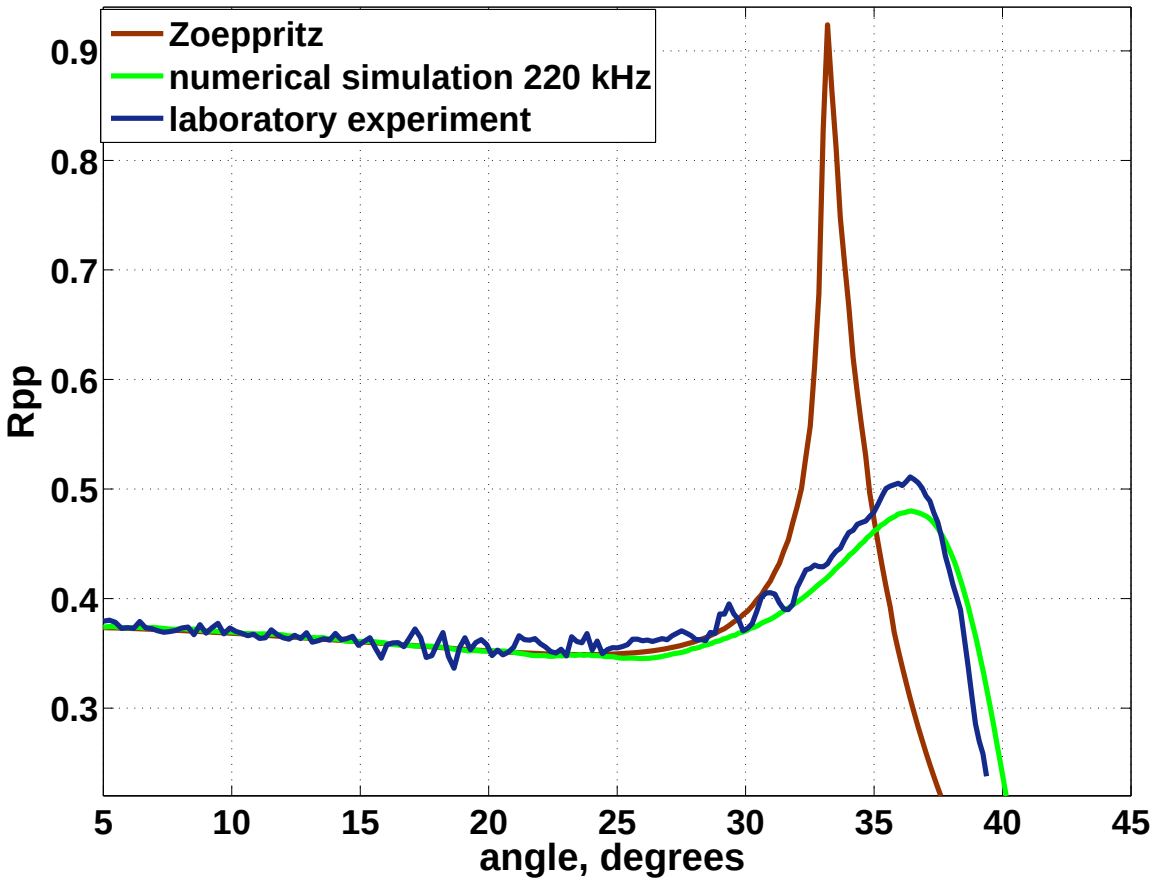

Figure 5.1 Comparison of measured reflection coefficients versus incidence angle for water/Plexiglas interface (blue line) with plane-wave response computed with Zoeppritz equations (brown line) and point-source numerical simulation (green line).

We can see an excellent agreement between laboratory-measured AVO response for the water/Plexiglas interface and numerical simulations. This indicates that the laboratory measurements were accurate, and the spherical approximation of the radiation pattern of the transducers was appropriate. This excellent match confirms the effect of a spherical wave on its AVO response and how it differs from that of a plane wave.

To analyze the effect of this difference on the AVO attributes in Figure 5.2 I re-plotted both experimental and theoretical reflection coefficients (for plane and spherical waves) against $\sin^2\theta$. We see that spherical and plane wave AVO responses show almost the same intercept and gradient, but very different curvature terms.

The agreement for small offsets is understandable; as the reflector is well in the far field (depth-to-wavelength ratio is about 36). However, somewhat surprisingly, we find that the far field (or high-frequency) approximation is still invalid at larger angles. To understand this effect we investigated it further by simulating the point-source AVA response at different frequencies.

The results for frequencies 50, 100, 220, and 400 kHz are plotted against $\sin^2\theta$ in Figure 5.3. The curves show no difference in intercept and gradient terms, but the curvature at larger angles (over 25º) is frequency dependent. Thus we expect that the frequency dependency of reflection coefficients will not affect conventional two-term AVO analysis, but it can distort the results of a three-parameter inversion if the later is performed using plane-wave Zoeppritz equations or its linear approximations.

5.3 Three-term AVO inversion

To analyze the effect of frequency on parameter extraction from reflection coefficients I implemented a least-mean-square inversion routine that attempts to find the medium parameters that give the best match between a given AVA curve (experimental or simulated) and Zoeppritz plane-wave solution.

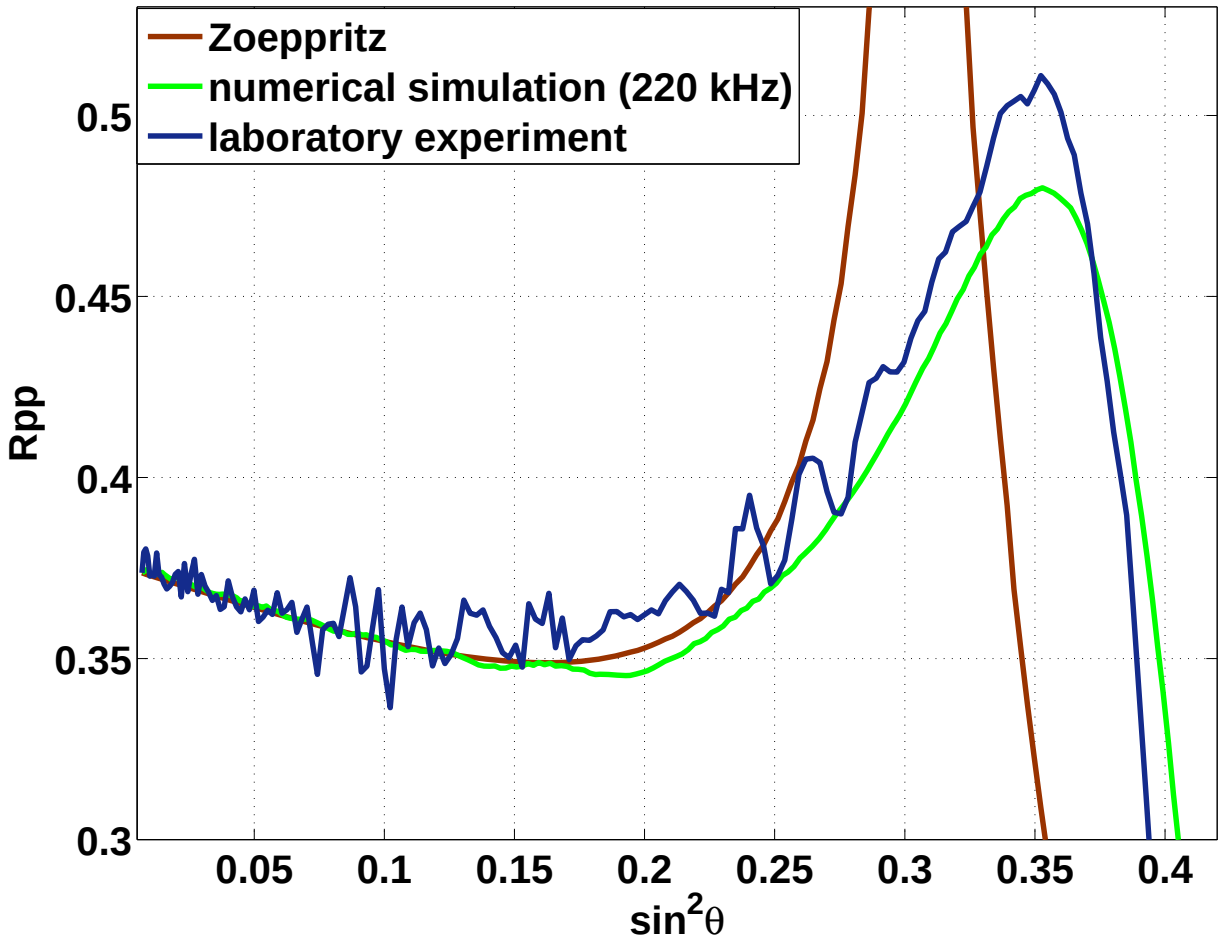

Figure 5.2 Comparison of measured reflection coefficients vs. $\sin^2\theta$ for water/Plexiglas interface(blue line) with plane-wave response computed with Zoeppritz equations (brown line) and point-source numerical simulation (green line).

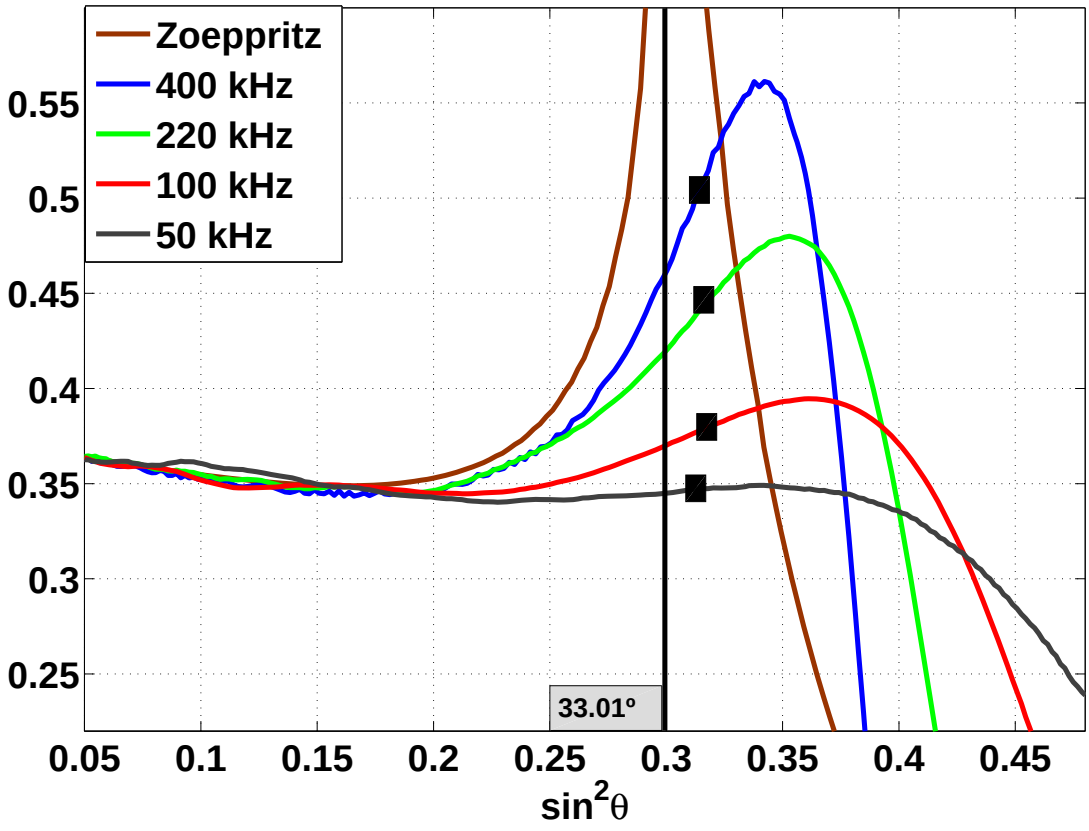

Figure 5.3 Simulated AVA responses at different frequencies plotted against $\sin^2\theta$. Squares denote inflection points used to estimate critical angles. Brown line is the plane-wave response computed with the Zoeppritz equations.

In this single-interface inversion I search for three parameters of the lower medium: P and S-wave velocities V_P and V_S, and density ρ, assuming that the properties of the upper medium V_{P0}, V_{S0}, and ρ_0 are known.

The spherical wave AVO responses at different frequencies along with the best plane-wave approximations are shown in Figure 5.4. The extracted parameters (V_P, V_S, ρ, as well as P and S impedances Z_P and Z_S) are listed in Table 5.1. It can be seen from Figure 5.5 that as the frequency decreases, the extracted impedances show little variation (<1% for Z_P and <4% for Z_S) whereas V_P, V_S and density show strong variation (up to 20%).

5.4 Inversion using critical angles

The fact that extraction of impedances is more robust than simultaneous extraction of velocities and densities is well known, as at moderate offsets the reflection coefficients are mainly sensitive to P and S impedance contrasts. In order to extract all three parameters we have to use large offsets where reflection amplitudes differ from the plane-wave response.

One way to overcome this difficulty is to use information about the critical angle. Critical angle corresponds to the singularity of the plane-wave reflection coefficient, and the first idea is to pick the maximum of the AVA curve. However, as we see in Figure 5.3, the position of the peak of R_{pp} also varies with frequency. However, recently Landro and Tsvankin (2007) suggested that the position of the inflection point (the point of the fastest increase) of the AVA curve is more stable and is a good proxy for the critical angle.

To reduce the parameter extraction errors caused by the spherical wave effects, we propose incorporating critical angles as measured by the position of the inflection point on AVA curves. The proposed workflow is as follows:

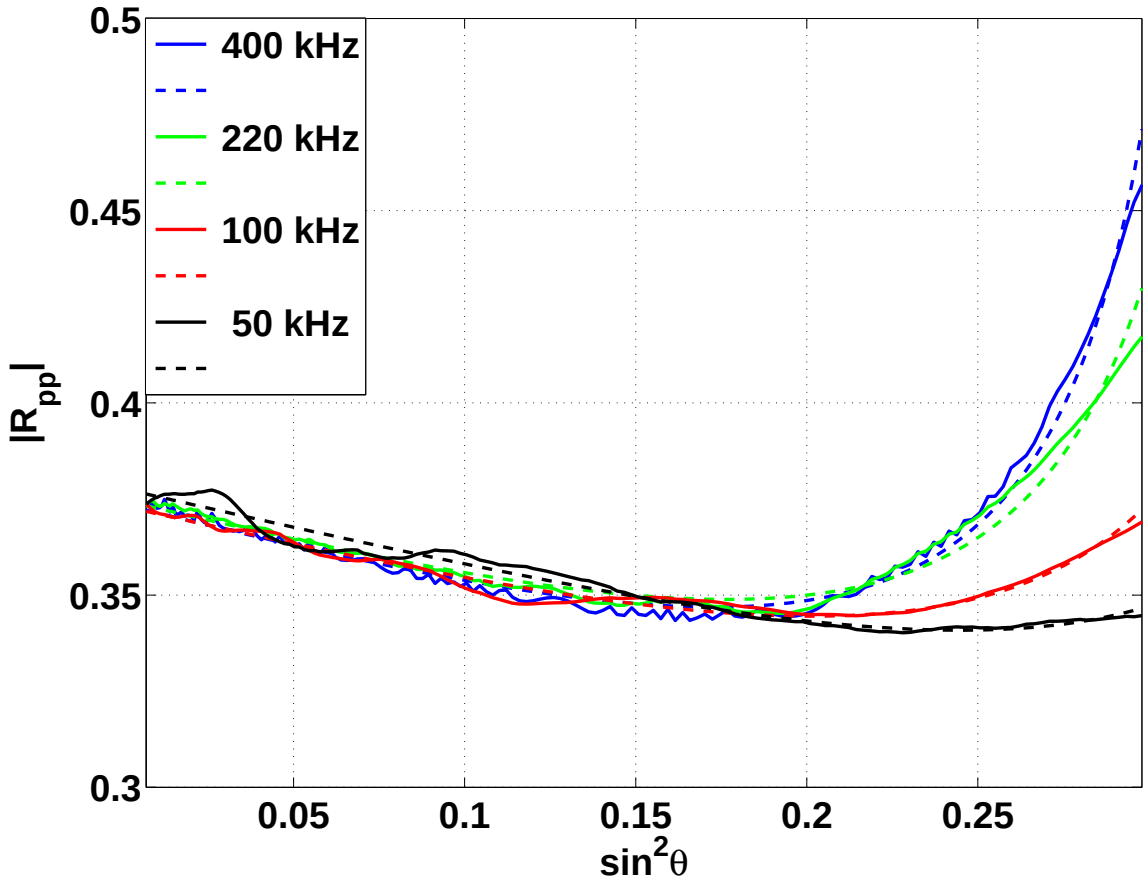

Figure 5.4 The spherical wave AVA responses at different frequencies along with the best-fit plane-wave approximations.

Parameters	V_P	V_S	ρ	Z_P	Z_S
True values	2.724	1.384	1.2	3.269	1.661
400 kHz	2.635	1.327	1.237	3.259	1.642
220 kHz	2.580	1.280	1.266	3.267	1.621
100 kHz	2.435	1.188	1.337	3.256	1.589
50 kHz	2.294	1.123	1.434	3.290	1.611
Laboratory	2.549	1.187	1.278	3.257	1.516

Table 5.1 Extracted parameters using three-term AVO inversion.

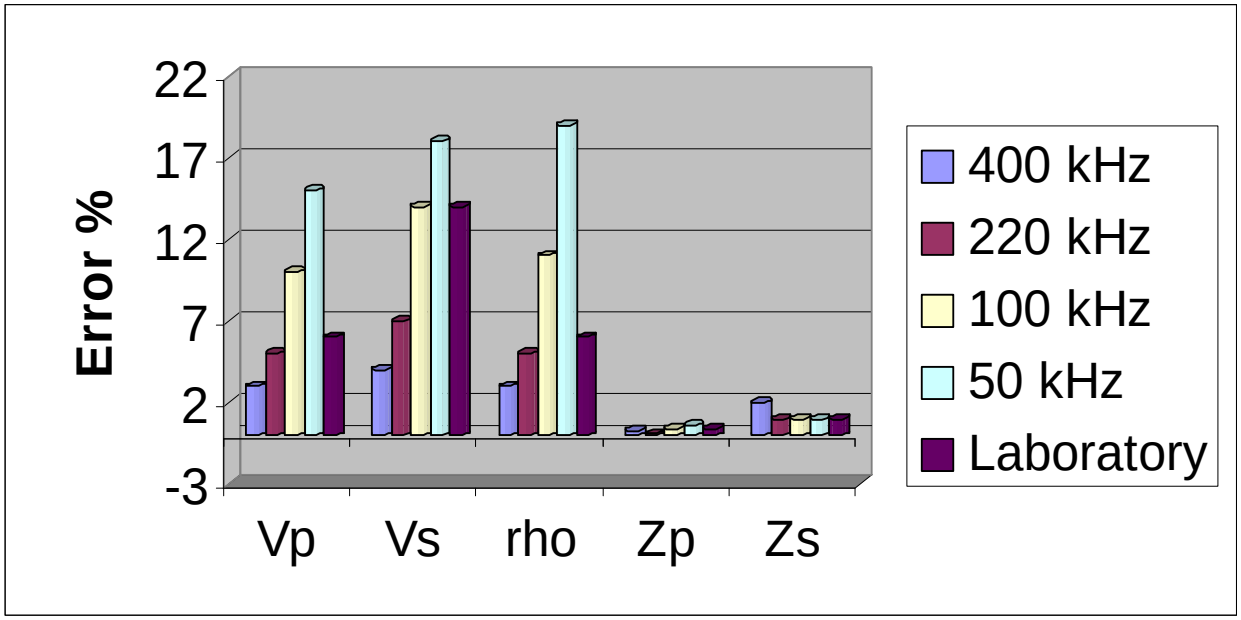

Figure 5.5 Variation of extracted parameters using thee-term AVO inversion from true values shown in error %.

1. Critical angle θ_{cr} is picked from the AVA curve as the angle corresponding to the inflection point.
2. P-wave velocity of the lower medium is computed using the Snell's law: $V_P = V_{P0}/\sin\theta_{cr}$.
3. Plane-wave inversion routine is used to extract P- and S- impedances only (by least-square fitting of plane-wave AVA (Zoeppritz) solution to the observed reflection coefficients for angles up to 20º).
4. Density is calculated as $\rho = Z_P/V_P$.
5. V_S is computed from Zs and density: $V_S = Z_S/\rho$.

I applied the above methodology to both numerically simulated and experimental AVA curves shown in Figures 5.2 and 5.3. The inflection points are shown on AVA curves of Figure 5.3. The extracted parameters are presented in Table 5.2. We can see that the critical angle based inversion method gives much better estimates of all three parameters than the curvature-based method (Figure 5.6). The errors in any parameters do not exceed 5%, except for the lowest frequency of 50 kHz.

An obvious limitation of the proposed technique is the requirement of a large and positive contrast between the velocities of the upper and lower media ($V_P > V_{P0}$). Of course we need long offsets and good signal to noise ratio. Careful and special processing steps are needed to preserve the true long offset reflected amplitudes. In the case of too low frequency, critical angles are hard to pick since the fastest amplitude increase is not evident even for noise-free numerical simulations (see the example for 50 kHz frequency, Figure 5.3).

Parameters	V_P	V_S	ρ	Z_P	Z_S
True values	2.724	1.384	1.2	3.269	1.661
400 kHz	2.689	1.399	1.217	3.272	1.702
220 kHz	2.691	1.392	1.219	3.280	1.697
100 kHz	2.694	1.308	1.211	3.262	1.583
50 kHz	2.707	1.471	1.223	3.309	1.799
Laboratory	2.704	1.380	1.217	3.292	1.680

Table 5.2 Extracted parameters using the new inversion method.

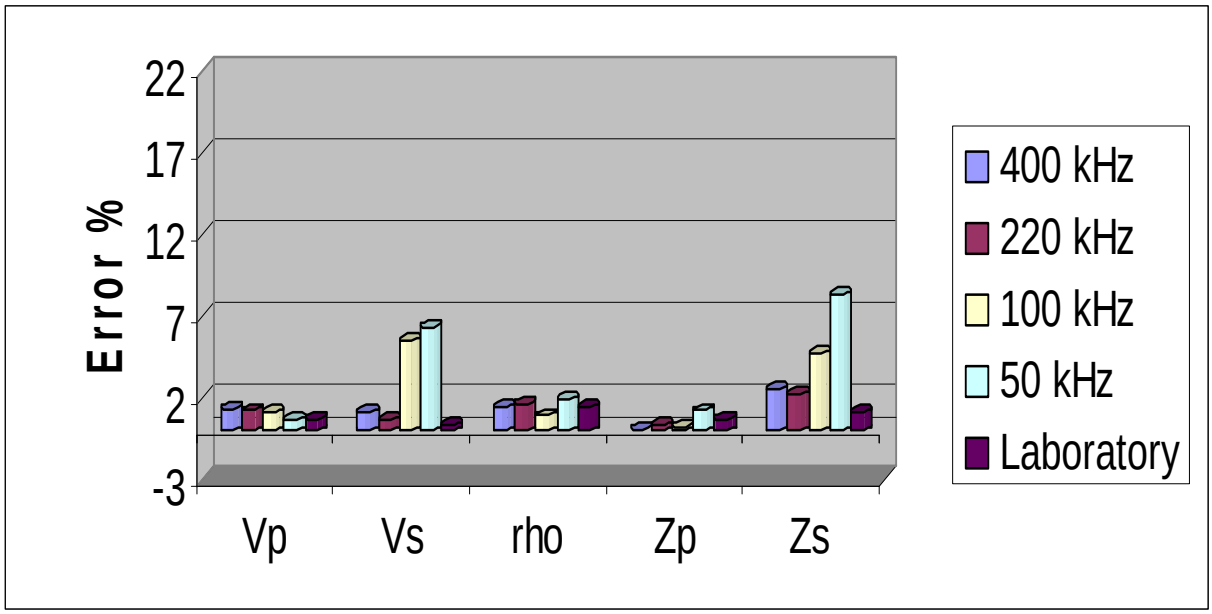

Figure 5.6 Variation of extracted parameters using the new inversion method (using critical angles) from true values shown in error %.

A different methodology of AVO inversion based on the transformation of common-shot gathers to plane-wave gathers using the tau-p transform was recently proposed by Van der Baan and Smit (2006). This is a promising approach for multi-layered elastic inversion.

5.5 Summary

P-P reflection coefficients measured in the laboratory for a water/Plexiglas interface show substantial deviation from the plane-wave reflection coefficients at large angles.
This deviation is explained by spherical wave effects, as demonstrated by full-wave point-source reflectivity simulations, which show excellent agreement with the laboratory experiments. The results demonstrate that the spherical wave effects can distort the results of three-term AVO inversion based on the AVA curvature. An alternative approach is to use critical angle information extracted from AVA curves and this leads to a significant improvement of the parameter estimation.

Chapter 6

AVOAZ RESPONSE OF A FRACTURED MEDIUM

6.1 Introduction

Fracture networks in a reservoir usually determine the direction and the amount of fluid flow. They can be open fractures and contribute positively by increasing permeability. On the other hand, they can act as a barrier to fluids when they are sealed. Therefore, detecting fracture orientation and intensity by studying azimuthal anisotropy in seismic data can be of crucial importance to hydrocarbon exploration.

In this chapter the AVOaz laboratory experiment results (from Chapter 3) are compared to numerical simulations using an anisotropic full-wave reflectivity algorithm. The comparison is done in terms of reflection amplitudes and critical angles extracted by picking inflection points on AVO curves for each azimuth.

6.2 Experimental results

The AVOaz experiment described in Chapter 3.5.2 produced seven seismograms, one for each recording azimuth. R_{pp} amplitudes for water/HTI interface were picked, calibrated and plotted against angle and azimuth as shown in Figure 6.1. The following features can be observed in this figure:

- Fracture induced anisotropy has a negligible effect on amplitudes for incidence angles up to 25 degrees. This focused the analysis towards large angle/offset reflection coefficients close to the critical angle.

- The reflection amplitude peak (close to the critical angle) shifts towards larger incidence angles from azimuths 0º to 45º, and then reverts back to its original position for azimuths 45º to 90º.

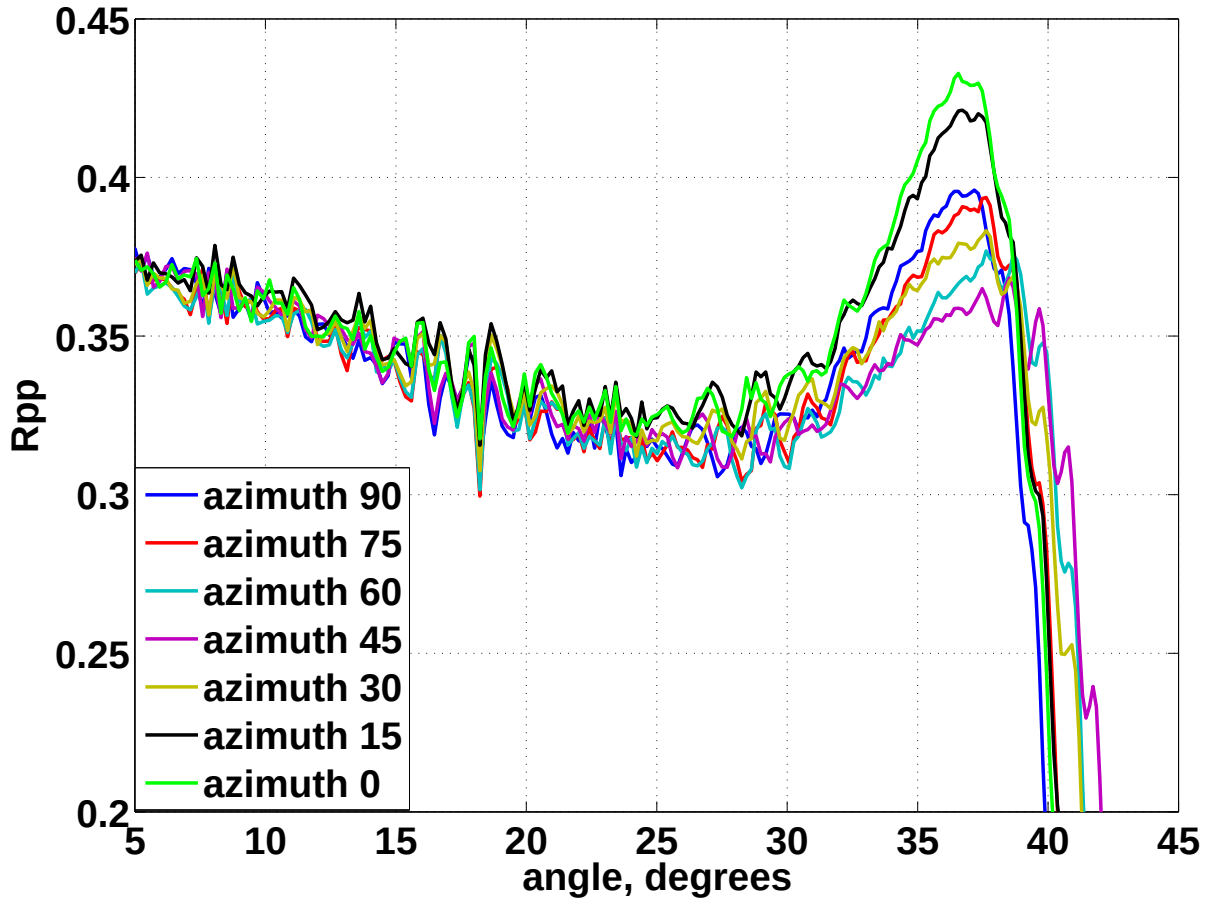

Figure 6.1 Laboratory experiment R_{pp} amplitudes for different azimuths plotted against angles of incidence.

6.3 Numerical simulations

The elastic parameters extracted from transmission measurements were used as an input to numerical simulation algorithms. The first idea was to compute plane-wave AVOaz reflection response for the water/HTI model interface using the anisotropic Zoeppritz equations (Schoenberg and Potazio, 1992). However, it is clear from analysis of Figures 5.1 and 6.1 that the azimuthal variation can only be observed at offsets where the match of the measured reflection coefficients with the theoretical plane-wave solution is affected by spherical wave.

In order to make a precise quantitative comparison between experiment and theory, I looked for a full-wave algorithm to simulate the anisotropic AVOaz responses numerically since this code is not available at Curtin University. British Geological Survey (BGS) has anisotropic full-wave reflectivity code and they kindly agreed to help me with the numerical simulation. I personally contacted Mr.Enru Liu and sent him the data (elastic properties and acquisition geometry).

The simulations were performed for a point source with a spherically symmetric radiation pattern. I obtained a series of CMP seismograms for each recording azimuth. Then, the amplitudes were picked on the seismic traces in the same manner as on the experimental traces. The resulting reflection coefficients are shown in Figures 6.2. It can be observed that reflection amplitudes do not change with azimuth for incident angles up to 25 degrees and the variation is limited to large angles. This agrees very will with the experimental results. In the next section a direct comparison between laboratory measurements and numerical simulations is done.

6.4 Comparison of laboratory experiments and numerical simulations

Now we compare the two sets of AVOaz curves as shown in Figures 6.3 a to g. The two data sets of AVOaz curves obtained from laboratory experiment and numerical

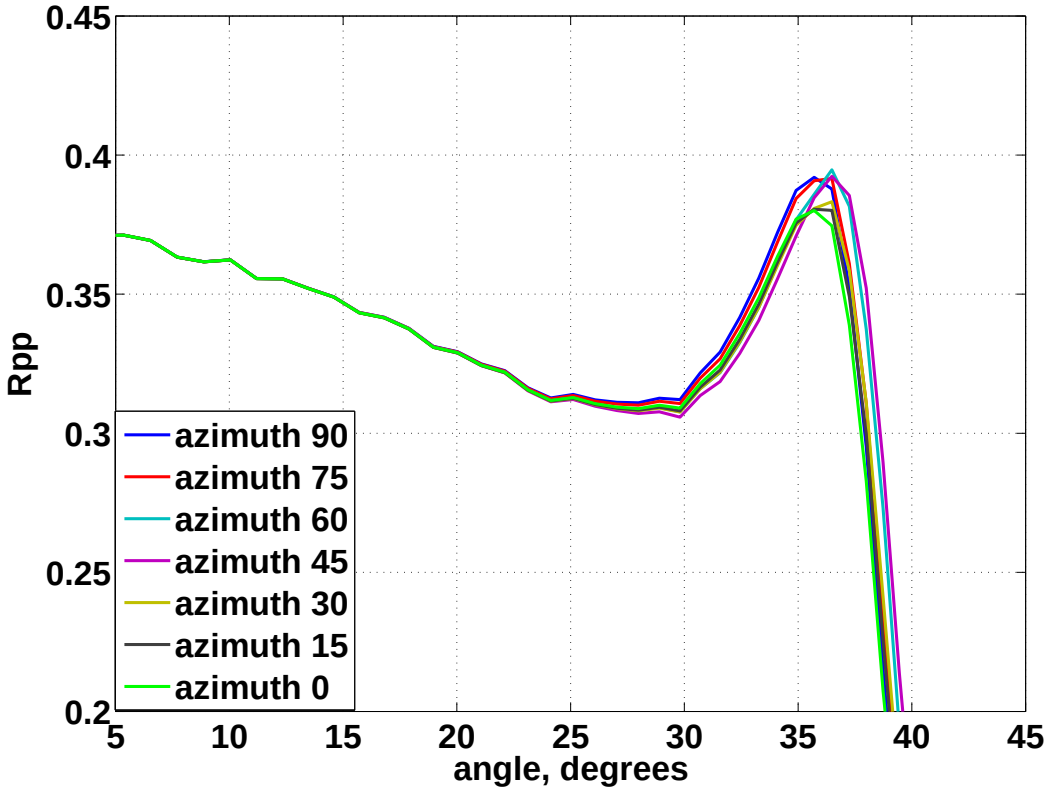

Figure 6.2 Numerical simulation R_{PP} amplitudes for different azimuths plotted against angles of incidence.

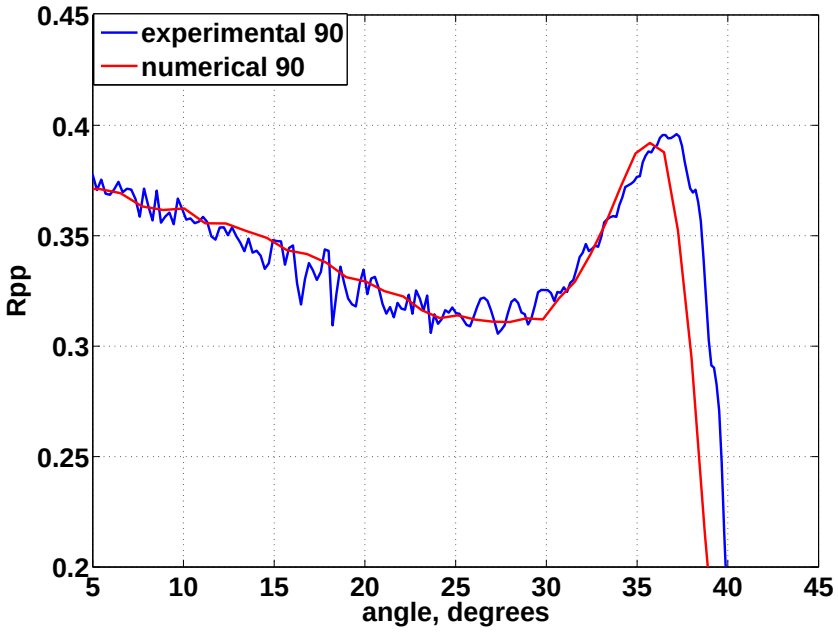

(a)

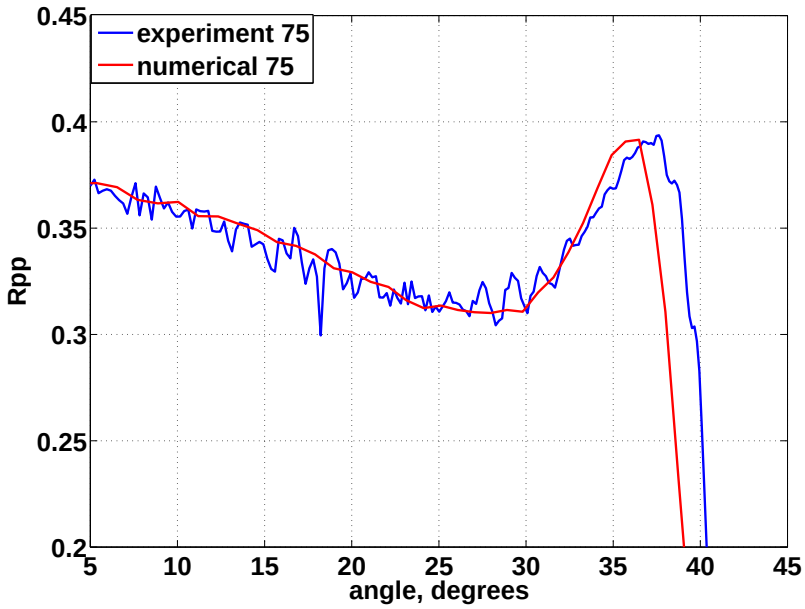

(b)

Figure 6.3 Comparison between laboratory measurement AVA curves and numerical simulations at different azimuths.

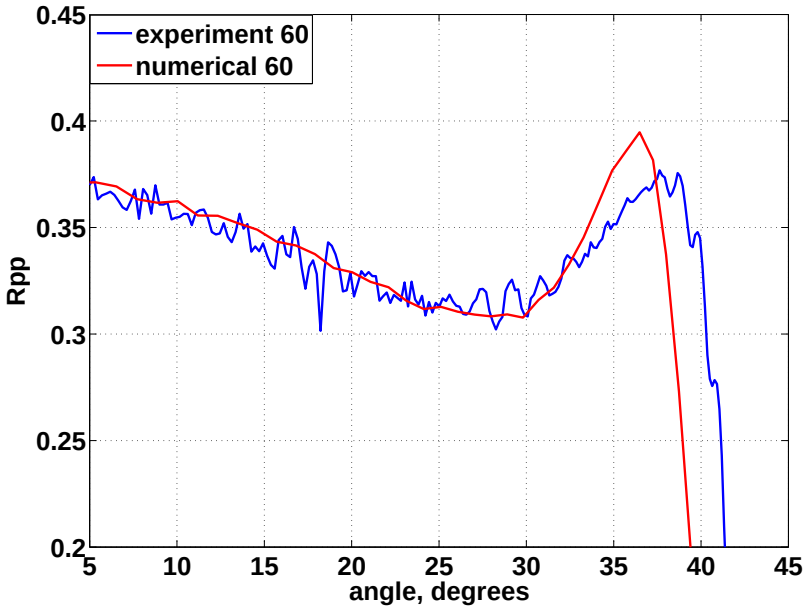

(c)

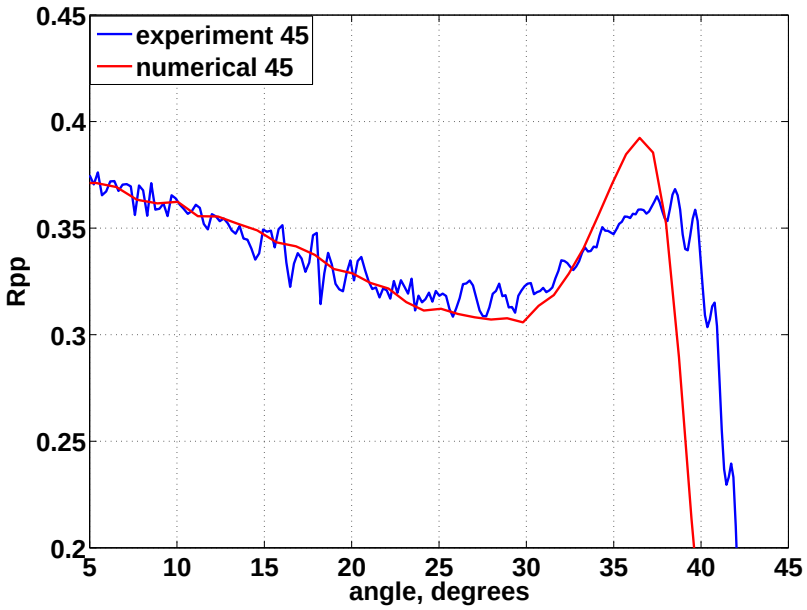

(d)

Figure 6.3 Comparison between laboratory measurement AVA curves and numerical simulations at different azimuths

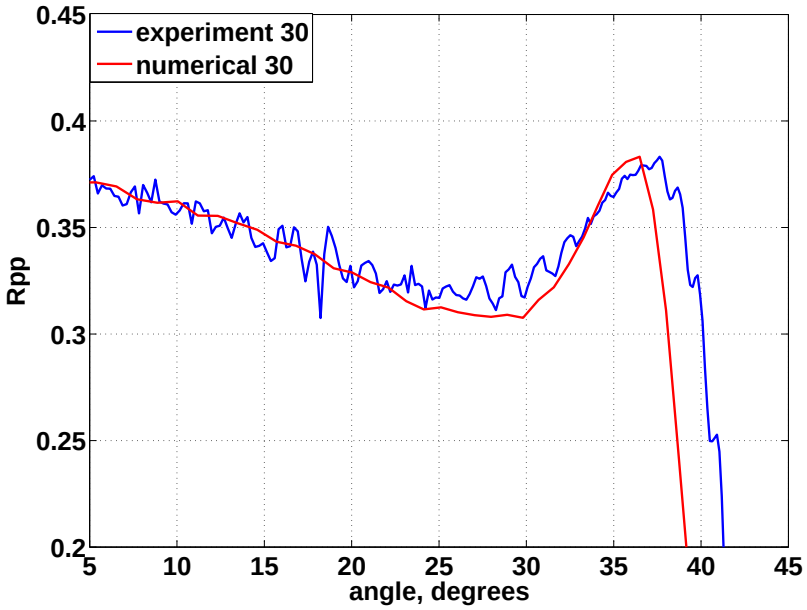

(e)

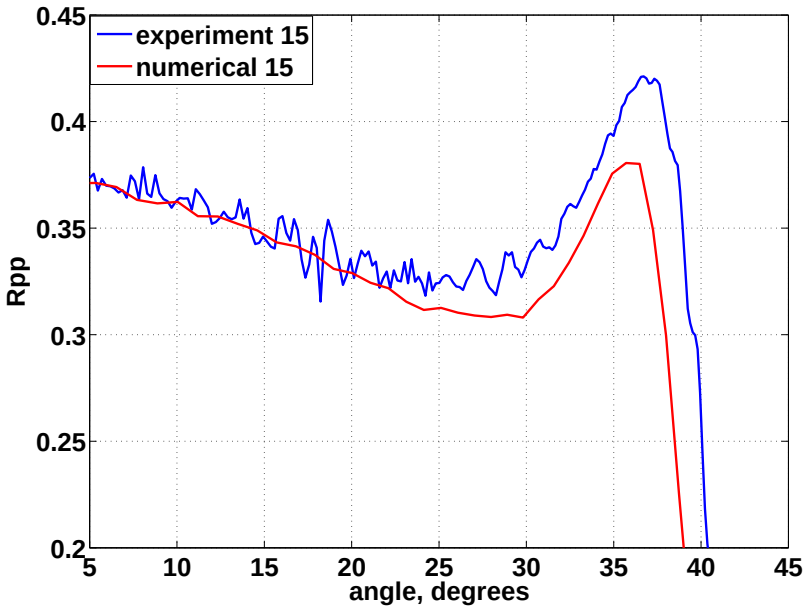

(f)

Figure 6.3 Comparison between laboratory measurement AVA curves and numerical simulations at different azimuths.

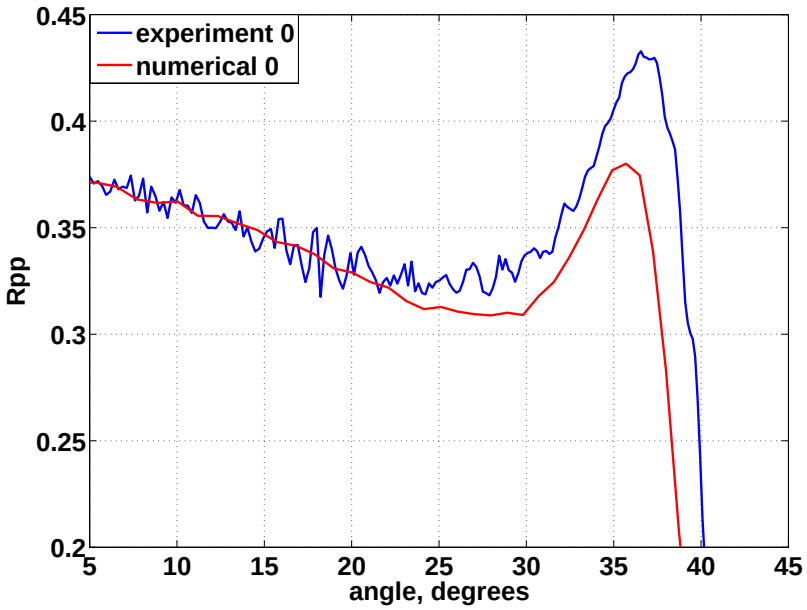

(g)

Figure 6.3 Comparison between laboratory measurement AVA curves and numerical simulations at different azimuths.

simulations have good agreement for azimuths 90º, 75º. On the other hand, the correlation deteriorates as azimuths get closer to the symmetry axis. At 15º and 0º azimuth, the physical modelling data show higher amplitude (by up to 7.5%), especially for large incidence angles. Possible reasons for the discrepancy are as follows:

- Finite fracture separation (violation of the effective medium approximation).
- Possible spatial heterogeneity of the model caused by the fact that the stress exerted by brackets used to hold Plexiglas sheets together is not uniform.
- Effect of the edges of the rectangular Plexiglas model.

One way to mitigate the effect of amplitude distortions is to analyze the azimuthal variation of the critical angle (Karrenbach et al., 1997, Landro and Tsvankin, 2007). Landro and Tsvankin (2007) suggested that a robust method of picking a critical angle from the AVOaz curves is to pick the point of the fastest amplitude increase of the reflection coefficient.

Critical angles calculated from the laboratory experiments and numerical simulations using this technique are shown in Figure 6.4. Also shown is plane-wave critical angles computed from the equation:

$$\frac{\sin\theta_{cr}}{V_{p1}} = \frac{1}{V_{p2}(\phi)} \quad , \tag{1}$$

where θ_{cr} is the critical angle, V_{p1} is the velocity of the upper medium (water), and $V_{p2}(\phi)$ is the phase velocity as a function of azimuth which can be calculated in terms of anisotropic parameters(Mavko, 1998):

$$V_{p2}(\phi) \approx \alpha(1+\delta\sin^2\phi\cos^2\phi+\varepsilon\sin^4\phi)\,, \tag{2}$$

where α is P-wave velocity along the symmetry axis, ε and δ are anisotropic parameters extracted from transmission measurements. All curves are nearly symmetric about 45º azimuth, which is expected for a liquid-filled fractured medium with

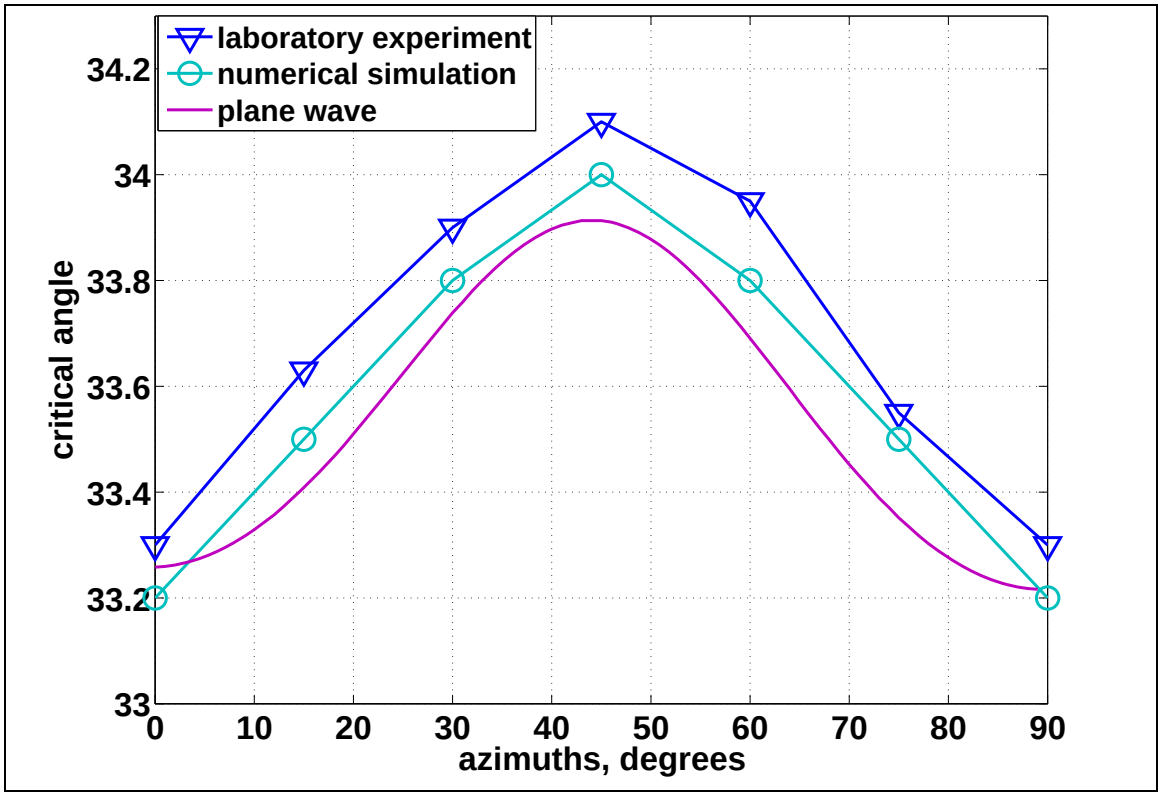

Figure 6.4 Comparison between critical angles computed from laboratory experiments, numerical simulations, and plane wave solutions at different azimuths.

very small ε (Rüger and Tsvankin, 1997). Minor asymmetry is caused by a minor difference in P-wave velocity parallel (2709 m/s) and perpendicular (2704 m/s) to the fractures. An excellent agreement is observed between the three critical angle curves.

6.5 Summary

The comparison of the experimental data with simulations shows that (1) reflection measurements are consistent with the transmission measurements (which are used as input into numerical simulations); (2) the anisotropic numerical simulation algorithm is capable of simulating subtle azimuthal variations with excellent accuracy; (3) the methodology of picking critical angles on seismograms using the inflection point is robust, even in the presence of random and/or systematic noise.

Chapter 7

Conclusions and recommendations

7.1 Conclusions

A spherical wave AVO response is investigated by measuring ultrasonic reflection amplitudes from a water/Plexiglas interface. The experimental results show substantial deviation from the plane-wave reflection coefficients at large angles. However there is an excellent agreement between experimental data and full-wave numerical simulations performed with the reflectivity algorithm. By comparing the spherical-wave AVO response, modelled with different frequencies, to the plane-wave response, I showed that the differences between the two are of such magnitude that three-term AVO inversion based on the AVA curvature can be erroneous. I then proposed an alternative approach to use critical angle information extracted from AVA curves, and showed that this leads to a significant improvement of the estimation of elastic parameters.

Azimuthal variation of the AVO response of fractured reservoirs is also usually modelled using equations for reflection coefficients obtained for plane waves. However, the plane wave approximation can break down at long offsets where incidence angle approaches the critical angle. Since azimuthal variation of AVO response is often more noticeable at large offsets (and can be rather weak), spherical wave effects must be carefully analysed and taken into account.

In order to analyse these effects quantitatively I performed an AVOaz laboratory experiment under fully controlled conditions, and then numerically simulated this experiment. The AVOaz response of a physical model was studied in the laboratory with finely layered Plexiglas simulating vertical fractures. Transmission measurements were performed to construct the elasticity tensor for the HTI model. This elasticity tensor was used as an input into numerical simulations which were performed using an anisotropic full-wave reflectivity algorithm.

The comparison of the experimental data with simulations showed a very good match for the isotropic case and good qualitative agreement for the azimuthal variations. The agreement is especially good for critical angles extracted by picking inflection points on AVO curves for each azimuth. This showed that (1) reflection measurements are consistent with the transmission measurements; (2) the anisotropic numerical simulation algorithm is capable of simulating subtle azimuthal variations with excellent accuracy; (3) the methodology of picking critical angles on seismograms using the inflection point is robust, even in the presence of random and/or systematic noise.

7.2 Recommendations

This research has demonstrated that the spherical wave effect on the AVO reflection response can cause inaccurate three-term nonlinear inversions where large offsets/incidence angles are included in the process. I recommend using an alternative inversion technique where critical angles are incorporated in the inversion process which results in a significant improvement in the estimation of true medium parameters.

I suggest that spherical wave effects must be carefully analysed and taken into account when interpreting the azimuthal variation of the AVO response of vertically fractured reservoirs. Critical angles at different azimuths could give valuable information about fractures direction and fluid content. In this research, critical angles at azimuths parallel and normal to the fractures are equal which indicated fluid filled fractures where the anisotropic parameter (Epsilon) is close to zero. It was impossible to distinguish the fractures' direction at 0 and 90 degree azimuths. Only 45 degree azimuth was known since the critical angle corresponded to the lowest value at that azimuth. I believe if we have dry fracture fill (gas) it will be possible to identify both fracture direction and fluid content since for the dry case, the anisotropic parameter (Epsilon) is not zero as shown by Rüger and Tsvankin (1997). This implies different critical angles at each azimuth and distinguishing the fracture orientation is not problematic anymore.

What I would like to do next is to apply this technique on real field data and test how robust the method is. If all the requirements for critical angles to be recorded and preserved in the azimuthal AVA curves are met, I want to know if it is feasible to sense such small variations in critical angles at different azimuths especially in the presence of noise and other factors, such as low signal-to-noise ratios and variable source/receiver radiation patterns.

REFERENCES

Aki, K. I. and Richards, P. G., 1980, Quantitative seismology: W. H. Freeman and Co.

Armstrong, P. N., W. Chmela, and W. S. Leaney, 1995, AVO calibration using borehole data: First Break, **13** , 319-328.

Backus, M., 1962, Long-wave elastic anisotropy produced by horizontal layering: J. Geophys. Res., 67, 4427-4440.

Bortfeld, R., 1961, Approximation to the reflection and transmission coefficients of plane longitudinal and transverse waves: Geophys. Prosp., **9**, 485-502.

Červený,V., 1961, The amplitude curves of reflected harmonic waves around the critical point: Studia Geophysica et Geodaetica, **5**, 319–351.

Crampin, S., E. M., Chesnokov, and R. A. Hipkin, 1984, Seismic anisotropy– the state of the art: First Break, **2**, 9-18.

Doruelo, J., F. Hilterman, and G. Goloshubin, 2004, Head waves as mechanism for azimuthal PP AVO magnitude anomalies: 76th Annual International Meeting, SEG, Expanded Abstracts, 199-202.

Downton, J. E., and C. Ursenbach, 2006, Linearized amplitude variation with offset (AVO) inversion with supercritical angles: Geophysics, **71**, E49-E55.

Ebrom D. A., and R. E. Sheriff, 1992, Anisotropy and reservoir development, in Sheriff, R. E, Ed, Reservoir Geophysics: SEG, Tulsa, 355-361.

Fatkhan, 2003, The modelling of elastic-wave amplitudes in anisotropic media: PhD thesis, Curtin University of Technology.

Fatkhan, M. Urosevic, and J. A. McDonald, 2001, Numerical and physical modelling of P-wave AVO response for fractured media: Exploration Geophysics, **32**, 279-285.

Gassmann, F., 1964, Introduction of seismic travel time methods in anisotropic media: Pure Applied Geophysics, **58**, 53-112.

Haase, A. B., 2004, Spherical wave AVO modeling of converted waves in isotropic media: 74th Annual International Meeting, SEG, Expanded Abstracts, 263-266.

Hornby, B. E., L. M. Schwartz, and J. A. Hudson, 1994, Anisotropic effective-medium modeling of the elastic properties of shales: Geophysics, **59**, 1570-1583.

Karrenbach, M., D. Nickols, and F. Muir, 1997, Modeling reflections from the Austin Chalk-apractical application of azimuthal anisotropy: SEP, **75**, http://sepwww.stanford.edu/public/docs/sep75/martin1/paper_html/index.html.

Kelly, M., C. Skidmore, and D. Ford, 2001, AVO inversion, Part 1: Isolating rock property contrasts: The Leading Edge, **20**, 230-323.

Krail, P. M., and H. Brysk, 1983, Reflection of spherical seismic waves in elastic layered media: Geophysics, **48**, 655-664.

Landro, M, 2007, Attenuation of seismic water-column noise tested on seismic data from the Grane field: Geophysics, **72**, no. 4, V87-V95.

Landro, M., and I. Tsvankin, 2007, Seismic critical-angle reflectometry?: A method to characterize azimuthal anisotropy: Geophysics, **72**, D41-D50.

Luo, M., and B. J. Evans, 2004, An amplitude-based multiazimuth approach to mapping fractures using P-wave 3D seismic data: Geophysics, **69**, 690-698.

MacCollum, B., and Snelll, F. A., 1932, Asymmetry of sound velocity in stratified formation: Trans. Petr. Geophysics, **2**,216-227.

Martin, M. A., T. L. Davis, 1987, Shear-wave birefringence: A new tool for evaluating fractured reservoirs: The Leading Edge, **6**, 22-28.

Mavko, G., 2001, Rock Physics for reservoir characterization and recovery monitoring: PESA short course, Perth, Australia.

Mavko, G., T. Mukeji, and J. Dvorkin, 1998, The rock physics handbook: Cambridge University Press.

Officer, C. B., 1958, Introduction to the theory of sound transmission with application to the ocean: McGraw-Hill Book Co.

Panametric,s, 1987, Model 5055PR pulser/receiver manual.

Rüger, A.,1996, Reflection coefficients and azimuthal AVO analysis in anisotropic media: PhD thesis, Colorado School of Mines.

Rüger, A.,2001, Reflection coefficients and azimuthal AVO analysis in anisotropic media: Geophysical monograph series, **10**, SEG.

Rüger, A., and I. Tsvankin, 1997, Using AVO for fracture detection: Analytic basis and practical solutions: The Leading Edge, 16, 1429-1434.

Schoenberg, M., and J. S. Protazio, 1992, Zoeppritz rationalized and generalized to anisotropy: Journal of Seismic Exploration, **1**, 125-144.

Sheriff, R. E., 1991, Encyclopaedic dictionary of exploration geophysics: SEG Publication.

Shuey, R. T., 1985, A simplification of the Zoeppritz equations: Geophysics, **50**, 609-614.

Slater, C., 1997, Estimation and modelling of anisotropy in vertical and walkaway seismic profiles at two North Caucasus oil fields: Ph.D. Dissertation, University of Edinburgh.

Smith, G. C., and P. M., Gidlow, 1987, Weighted stacking for rock property estimation and detection of gas: Geophys. Prosp., **35**, 993-1014.

Teng, L., and G. Mavko, 1996, Fracture signatures on P-wave AVOZ: 66th Annual International Meeting, SEG, Expanded Abstracts, 1818-1821.

Timoshenko, S., and J. N. Goodier, 1934, Theory of Elasticity: McGraw-Hill Book Co.

Thomsen, L., 1986, Weak elastic anisotropy: Geophysics, **51**, 1954-1966.

----------, 2002, Understanding seismic anisotropy in exploration and exploitation: Distinguished Instructor Short Course Notes, SEG.

Tsvankin, I., 2001, Seismic signatures and analysis of refection data in anisotropic media: Elsevier Science Publ. Co., Inc.

Urdaneta, H., 1997, Azimuthal behavior of P-waves in horizontal transverse isotropy: SEP, **92**, http://sepwww.stanford.edu/public/docs/sep92/hector1/paper_html/index.html.

Urosevic, M., 1985, Some effects of an anisotropic medium on P and SV wave: A physical modelling studies: M.Sc. thesis, University of Houston.

Van der Baan, M., and D. Smit, 2006, Amplitude analysis of isotropic P-wave reflections: Geophysics, **71**, C93-C103.

White, J. E., 1965, Seismic wave: radiation, transmission and attenuation: McGraw-Hill Book Co.

Winterstein, D. F., and J. B. Hanten, 1985, Supercritical reflections observed in P- and S-wave data: Geophysics, **50**, 185-195.

Yilmaz, O, 1987, Seismic Data Processing, vol. 2: SEG Publication.

Zoeppritz, K., 1919, On the reflection and propagation of seismic waves: Gottinger Nachrichten, **1**, 66-84.

APPENDICES

Appendix A

Three-term AVO inversion program

This is a least-mean-square inversion routine that attempts to find the medium parameters that give the best match between a given AVA curve (experimental or simulated) and Zoeppritz plane-wave solution. The program was written in Matlab and I copied it straight from the Matlab window as shown here:

Inversion

```
% P-wave reflection coefficient as function of angle
clear all;
global vp1 vs1 rho1 angles amp nangles

avofile='amplitudes.txt';
% avofile='plane.txt';
fileread=fopen(avofile,'r');
matr = fscanf(fileread,'%g',[5 inf]);
fclose(fileread);

s=size(matr);
cols=s(1);
nangles=s(2);
nangles=156;

angles=matr(1,:);

% for m=2:cols
%     plot(angles,matr(m,:),'LineWidth',2);
%     hold all;
%     grid on;
% end


vp1=1486; vs1=1; rho1=1000;

initpar=[2700,1400,1200];
initpar=[3000,1000,1000];
```

```
figure;
colstr='bgrkcmbwy';
f=[400 220 100 50];
for m=2:cols

    amp=matr(m,:);
%    [x,fval] =
fminsearch(@discrepancy,initpar,optimset('MaxIter',5));
    [x,fval] = fminsearch(@discrepancy,initpar);
    Vp2=x(1) ;
    Vs2=x(2);
    Rho2=x(3);
    Zp=Vp2*Rho2;
    Zs=Vs2*Rho2;
    err=fval;

    parmat(m-1,1)=Vp2/1e3;
    parmat(m-1,2)=Vs2/1e3;
    parmat(m-1,3)=Rho2/1e3;
    parmat(m-1,4)=Zp/1e6;
    parmat(m-1,5)=Zs/1e6;

    for n=1:nangles
        nurad=angles(n)*pi/180;
        R(n)=Zoeppritz(nurad,vp1,vs1,rho1,Vp2,Vs2,Rho2);
    end
    ang=angles(1:nangles);
    freq=sprintf('%4.0f',f(m-1));
    ispher=['-' colstr(m-1)];
    ifit=['--' colstr(m-1)];
    mp=(m-2)*2;
    leg(mp+1)={freq};
    leg(mp+2)={' '};
    plot(angles,amp,ispher,ang,abs(R),ifit,'LineWidth',2);
%
plot((sind(angles)).^2,amp,ispher,(sind(ang)).^2,abs(R),ifi
t,'LineWidth',2);
    grid on;
    hold on;
end
axis([angles(1) angles(nangles) 0.3 0.6])
% axis([sind(angles(1))^2 sind(angles(nangles))^2 0.3 0.5])
xlabel('Angle, degrees')
% xlabel('sin^2\theta')
ylabel('|R_{pp}|')
% title('Reflection coeffcieint as a function of angle')
legend(leg,'Location','EastOutside');
```

```
% H=gca; set(H,'MinorGridLineStyle', 'none');

Parmat
```

Discrepancy

```
function DD = discrepancy(x)

global vp1 vs1 rho1 angles amp nangles

S=0;
vp2=x(1);
vs2=x(2);
rho2=x(3);
for n=1:nangles
    nurad=angles(n)*pi/180;
    R=Zoeppritz(nurad,vp1,vs1,rho1,vp2,vs2,rho2);
    S=S+(abs(R)-amp(n))^2 * cos(nurad)^8;
    R1(n)=R;
end
% ang=angles(1:nangles);
% plot(ang,abs(R1),'-',angles,amp,'--','LineWidth',2);
% grid on;
% hold on;
if(rho2<=0)
    S=S+exp(abs(rho2));
end

if(vp2<=0)
    S=S+exp(abs(vp2));
end
if(vs2<=0)
    S=S+exp(abs(vs2));
end

N=nangles;
DD=S;
```

Zeoppritz

```
function Rpp = Zoeppritz(i1,vp1,vs1,rho1,vp2,vs2,rho2)

% Snell's law
p=sin(i1)/vp1;
i2=asin(p*vp2);
```

```
j1=asin(p*vs1);
j2=asin(p*vs2);

% Zoeppritz equations as writtern in Ruger 2002, pages 16-
17.
a=rho2*(1-2*vs2^2*p^2)-rho1*(1-2*vs1^2*p^2);
b=rho2*(1-2*vs2^2*p^2)+2*rho1*vs1^2*p^2;
c=rho1*(1-2*vs1^2*p^2)+2*rho2*vs2^2*p^2;
d=2*(rho2*vs2^2-rho1*vs1^2);

cosi1=cos(i1);
cosi2=cos(i2);
cosj1=cos(j1);
cosj2=cos(j2);

E=b*cosi1/vp1+c*cosi2/vp2;
F=b*cosj1/vs1+c*cosj2/vs2;
G=a-d*(cosi1/vp1)*(cosj2/vs2);
H=a-d*(cosi2/vp2)*(cosj1/vs1);

D=E*F+G*H*p^2;

Rpp=((b*cosi1/vp1-c*cosi2/vp2)*F-
(a+d*(cosi1/vp1)*(cosj2/vs2))*H*p^2)/D;
```

Reflection

```
% P-wave reflection coefficient as function of angle
clear all;
numin=0; nustep=1; numax=60;

vp1=1486; vs1=1; rho1=1000;
vp2=2724; vs2=1384; rho2=1200;

n=1;
for nu = numin:nustep:numax
%     [S,P,w,w1,Q,AA,V,r] = eval2N(N,cp,cs,rho,a,b,nu);
    nurad=nu*pi/180;
    R(n)=Zoeppritz(nurad,vp1,vs1,rho1,vp2,vs2,rho2);
    angle(n)=nu;
    n=n+1;
end

plot(angle,real(R),'-',angle,imag(R),'--',angle,abs(R),'-
.');
grid on;
```